

Generative Transformer for Accurate and Reliable Salient Object Detection

Yuxin Mao, Jing Zhang, Zhexiong Wan, Yuchao Dai*,
Aixuan Li, Yunqiu Lv, Xinyu Tian, Deng-Ping Fan and Nick Barnes

Abstract—Transformer, which originates from machine translation, is particularly powerful at modeling long-range dependencies. Currently, the transformer is making revolutionary progress in various vision tasks, leading to significant performance improvements compared with the convolutional neural network (CNN) based frameworks. In this paper, we conduct extensive research on exploiting the contributions of transformers for *accurate* and *reliable* salient object detection. For the former, we apply transformer to a deterministic model, and explain that the effective structure modeling and global context modeling abilities lead to its superior performance compared with the CNN based frameworks. For the latter, we observe that both CNN and transformer based frameworks suffer greatly from the over-confidence issue, where the models tend to generate wrong predictions with high confidence. To estimate the reliability degree of both CNN- and transformer-based frameworks, we further present a latent variable model, namely inferential generative adversarial network (iGAN), based on the generative adversarial network (GAN). The stochastic attribute of the latent variable makes it convenient to estimate the predictive uncertainty, serving as an auxiliary output to evaluate the reliability of model prediction. Different from the conventional GAN, which defines the distribution of the latent variable as fixed standard normal distribution $\mathcal{N}(0, \mathbf{I})$, the proposed “iGAN” infers the latent variable by gradient-based Markov Chain Monte Carlo (MCMC), namely Langevin dynamics, leading to an input-dependent latent variable model. We apply our proposed iGAN to both fully and weakly supervised salient object detection, and explain that iGAN within the transformer framework leads to both accurate and reliable salient object detection.

Index Terms—Vision Transformer, Salient Object Detection, Inferential Generative Adversarial Network.



1 INTRODUCTION

Visual salient object detection (SOD) [1]–[14] aims to localize and segment the regions of an image that attract human attention, which is usually defined as a binary segmentation task. Depending on whether unimodal data (*i.e.* RGB image) or multimodal data (*i.e.* RGB-D data) is used, the majority of salient object detection models can be roughly divided into RGB image saliency detection [2], [3], [12]–[14] and RGB-D image pair saliency detection [4], [5]. The former involves two variables, namely the RGB image x and its corresponding ground truth saliency map y , while the extra depth data d is involved in the latter, making it a multimodal learning task.

Given the one-to-one mapping formulation, and the backbone-dependent network structures, the main focus of conventional deep RGB image-based saliency detection models is achieving structure-preserving prediction with effective high/low level feature aggregation. On the other hand, as a multimodal learning task, the basic assumption of RGB-D saliency detection is that the extra depth data can bring informative geometric information, which can be complementary to the appearance information from the RGB image. In this case, the main focus of existing RGB-D

SOD models [5], [15]–[17] is to extensively utilize the geometric information for effective multimodal learning.

By thoroughly analyzing the existing saliency detection models, we observe three major issues, namely the less effective global context modeling abilities, the missing structure information issue, and the inconsistent depth distribution issue.

Less effective global context modeling: Conventional CNN based saliency detection models usually consist of two main parts: 1) an encoder for feature extraction; and 2) a decoder for high/low feature aggregation, where the encoder is usually adopted from an ImageNet pre-trained backbone network, *e.g.*, VGG [29], ResNet [18]. In this way, the SOD models are mainly designed to obtain effective decoders for feature aggregation [2], [3], [30]. We visualize the different levels of CNN and transformer backbone features of the SOD models in Fig. 1 and find that the former encodes less accurate global context than the latter, especially for the large salient foreground (the first row of Fig. 1).

Missing structure information: Conventional CNN backbones have gradually larger receptive fields with the deeper layers by using stride or pooling operation, leading to extensive down-sampling as shown in Fig. 1 (“CNN”), where we show the different levels of backbone features of the ResNet50 [18] after fine-tuning it for SOD. We observe missing structure information¹ in both higher and lower level features, which makes effective high/low feature aggregation especially necessary for CNN backbone based framework to achieve structure-accurate predictions. However, once the information is lost, it will not be fully recovered.

Inconsistent depth distribution: For RGB-D saliency detection,

1. We define “structure information” as the detail-alignment of prediction with the input image.

- Yuxin Mao, Zhexiong Wan, Yuchao Dai, Aixuan Li, Yunqiu Lv and Xinyu Tian are with School of Electronics and Information, Northwestern Polytechnical University, Xi’an, China.
- Jing Zhang and Nick Barnes are with School of Computing, Australian National University, Canberra, Australia.
- Deng-Ping Fan is with the CS, Nankai University, Tianjin, China.
- Corresponding author: Yuchao Dai (Email: daiyuchao@nwpu.edu.cn).
- The source code and experimental results are publicly available via our project page: <https://github.com/fupiao1998/TransformerSOD>.

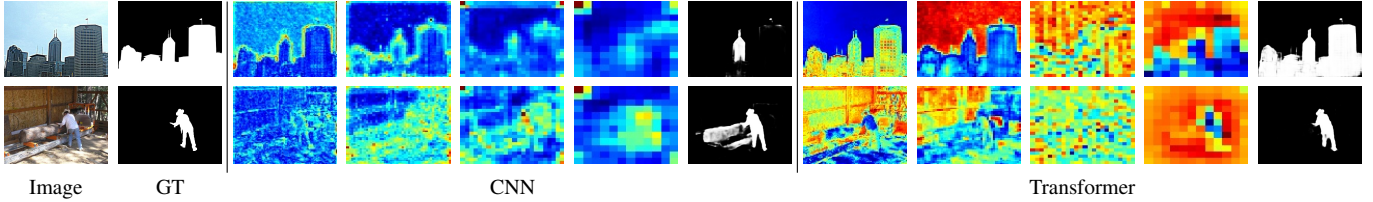


Fig. 1. Visualizing the features of the ResNet50 backbone [18] (“CNN”) and the transformer backbone (“Transformer”) after fine-tuning them for SOD.

TABLE 1
Details of the widely used RGB-D saliency datasets to explain the domain gap issue for RGB-D saliency detection.

Dataset	Year	Size	Type	Depth Source	#Train	#Test
SSB [19]	2012	1,000	Internet	Stereo cameras+ optical flow [20]	-	1,000
NLPR [21]	2014	1,000	Indoor/Outdoor	Microsoft Kinect [22]	700	300
DES [23]	2014	135	Indoor	Microsoft Kinect [22]	-	135
NJU2K [24]	2014	1,985	Movie/Internet	FujiW3 camera + Sum’s optical flow [25]	1,500	485
LFSO [26]	2014	80	Indoor/Outdoor	Lytro Illum cameras [27]	-	80
SIP [28]	2020	929	Person in outside	Huawei Mate10	-	929

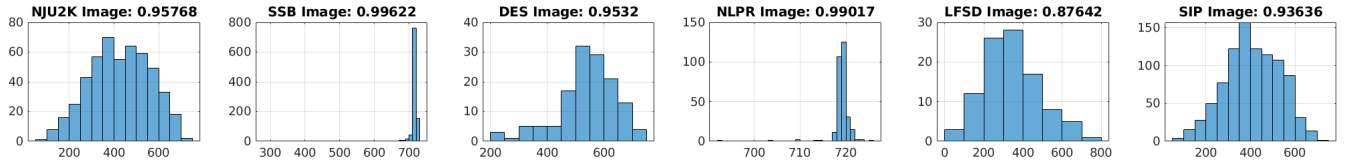


Fig. 2. Global contrast of depth from benchmark RGB-D SOD datasets, where the x-axis is the Chi-squared distance between salient foreground and non-salient background within the depth data, and the y-axis is the number of images.

extra depth data is involved, and the mainstream is then to effectively explore the complementary information of both modalities for effective multimodal learning. We observe that the depth data of RGB-D saliency detection can come from different sensors as shown in Table 1, thus the training data and the testing data can be treated as from different domains. Further, we find that depth from different sensors has different contrast distributions, leading to inconsistent input distributions across the training and testing datasets. We compute the global contrast of the depth data from different testing datasets and show the global depth contrast in Fig. 2. The global contrast measures the noticeability of the salient objects. To obtain the global contrast of the depth data, we first compute a $3H$ dimensional color histogram of both salient foreground and background of the depth data. Following [31], we obtain an $H = 16$ dimensional histogram for the Red, Green, and Blue channel² of the RGB image respectively, and the histogram of the color image is then the concatenation of the above histograms. Then we adopt the Chi-squared distance to measure the global contrast between salient objects and background. We define the mean of the Chi-squared distance as the global depth contrast. Fig. 2 clearly shows that the global contrast of the salient foreground with the depth data varies across the testing datasets. Similarly, we obtain the RGB image global contrast and compute the global contrast difference of the RGB image and depth for each testing dataset, which is shown in the title of each figure in Fig. 2. The various global contrast differences between RGB images and depth data further explain the different contributions of depth.

Advantages of Transformer: Researchers have found that the

“Transformer” [32] has great potential to solve the limited receptive field issue in vision tasks. The advantage of the “Transformer” lies in the use of self-attention to capture global contextual information to establish a long-range dependency. Different from convolutional neural networks that focus on a small patch of the image, the transformer network [32] performs global context modeling with self-attention. Inspired by [33], [34] and the accurate structure modeling ability of the transformer (see Fig. 1), we conduct extensive research to explore the contributions of the transformer for accurate salient object detection. Specifically, we design transformer based deterministic neural networks for SOD, and explain that the accurate structure modeling and the global context modeling abilities lead to its superior performance compared with the CNN based frameworks (see Table 5).

Overcoming the over-confidence issue: Although significant performance has been achieved with the transformer, we still observe “over-confidence” issue within the transformer based SOD models, where the model tends to generate wrong prediction with high confidence, which is also defined as the model less-calibrated issue in [35]. We then present an inferential generative adversarial network (iGAN) to analyze the reliability degree [35] of the transformer based framework. Different from the conventional generative adversarial network (GAN) [36] which defines the distribution of the latent variable as fixed standard normal distribution $\mathcal{N}(0, \mathbf{I})$, our proposed “iGAN” infers the latent variable by gradient based Markov Chain Monte Carlo (MCMC), namely Langevin dynamics [37]. The latent variable within iGAN is sampled directly from its true posterior distribution [38], leading to more informative latent space exploration. We apply the proposed iGAN to both fully and weakly supervised SOD, and explain that iGAN within the

2. For gray image, we obtain its color version by concatenating it channel-wise to obtain the three-channel color image.

transformer framework leads to both accurate and reliable salient object detection, where the produced uncertainty maps [39] can serve as an auxiliary output to explain the reliability of model predictions. Experimental results show that the proposed iGAN within the transformer backbone can fix the “less effective global context modeling” and “missing structure information” issues of conventional CNN backbone based framework, and the auxiliary uncertainty outputs can be used to explain model reliability.

Fixing the depth domain gap issue: Although consistent performance improvement is achieved with the transformer backbone based framework, we still observe the depth domain inconsistency issue, where the testing datasets with depth different from the training datasets achieve a marginal performance improvement, *e.g.* LFSD [26] in Fig. 2. To fix it, we present an “auxiliary depth” module and perform self-supervised depth estimation. The deep hybrid model structure [40] via depth reconstruction, *i.e.* RGB-D saliency detection as conditional generation and depth estimation as marginal density estimation, works effectively when a depth domain gap exists.

Our main contributions can be summarized as: **1)** We extensively explore the contributions of transformer networks [32]–[34], [41] for **accurate** salient object detection and explain that the effective structure and global context modeling abilities lead to the superior performance of the transformer-based saliency detection network; **2)** We present an inferential generative adversarial network (iGAN) to effectively measure the reliability degree of the transformer-based SOD network, leading to **reliable** saliency prediction; **3)** We apply iGAN to fully and weakly supervised salient object detection to extensively explore the proposed new generative model within the transformer framework.

2 RELATED WORK

Salient Object Detection: Driven by visual attention [42], salient objects are defined as objects that have strong contrast [43]. Early works usually utilized this prior for saliency related feature extraction. Deep SOD models usually take the pretrained backbone networks [18], [29] as an encoder with UNet [44] structure, where effective decoders are designed to achieve high-low level feature aggregation [2], [3], [30], [45]–[54]. Among them, Wu *et al.* [2] proposed a “stacked cross refinement network”, and used the interaction between the edge module and the detection module to optimize the two tasks at the same time. Wei *et al.* [3] introduced an adaptive selection of complementary information when aggregating multi-scale features with a structure-aware loss function. Tang *et al.* [55] modeled the two tasks of discriminating salient regions and identifying accurate edges independently and solved the limitations of low-resolution SOD by using low-resolution images to delineate salient regions and using high-resolution to refine salient regions. Meanwhile, edge detection [56], [57] is likewise used as a piece of auxiliary information [58], [59] to improve the performance of SOD. And different attention mechanisms such as spatial and channel attention [15], [60] or pixel-wise contextual attention [46] are also used to learn more discriminative features. Unlike the mainstream design refinement prediction networks, Zhang *et al.* [61] proposed an automatic consolidation of multi-level features based on neural architecture search for flexible integration of information at different scales.

With extra depth information, RGB-D pair based SOD models [4], [5], [15], [16], [62], [63] mainly focus on exploring the complementary information between the RGB image and the depth data for effective multi-modal learning. Depending on how

information from these two modalities is fused, existing RGB-D SOD models can be roughly divided into three categories: early-fusion models [4], [64], late-fusion models [65]–[67] and cross-level fusion models [5], [15], [17], [68]–[78]. The early-fusion models fuse RGB image and depth data at the input layer, forming a four-channel feature map. The late fusion models treat each mode (RGB and depth) separately, and then saliency fusion is achieved at the output layer. The cross-level fusion models gradually fuse features of RGB and depth [5], [17], [72], [73], [75], [77]–[83], which is the main stream for RGB-D SOD.

Vision Transformer and Its Applications: The transformer network [32] has sparked great interests in the computer vision community to adapt these models for vision tasks such as object detection [84]–[88], object tracking [89], [90], pose estimation [91], optical flow [92] *etc.* Inspired by the success of the Vision Transformer (ViT) [41] in image classification which splits the input image into a sequence of patches and feeds them to a standard Transformer encoder, some works extend transformers for dense prediction tasks, *e.g.*, semantic segmentation or depth estimation. SETR [93] and PVT [87] use several convolutional layers as the decoder to upsample feature maps and get the dense prediction with the input image size. DPT [33] uses ViT [41] as an encoder to extract features from different spatial resolutions of the initial embedding. Liu *et al.* [34] presented the Swin Transformer, a hierarchical transformer with a shifted windowing scheme to achieve an efficient network for vision tasks. Recently, [94], [95] introduce the transformer to saliency detection, achieving significant performance improvement.

Generative Models and Their Applications: There mainly exist two types of generative models, namely latent variable models [36], [96] and energy-based models [97]. The former usually involves an extra latent variable to model the predictive distribution, and the latter directly estimates the compatibility of the input and output variable with a designed energy function. The variational auto-encoder (VAE) [96], [98] and generative adversarial network (GAN) [36] are two widely studied latent variable models. VAEs use an extra inference model to constrain the distribution of the latent variable, and GANs design a discriminator to distinguish real samples and the generated samples. VAEs have already been successfully applied to image segmentation [99], [100] to produce stochastic predictions during testing. For saliency prediction, [101] adopts a VAE for image background reconstruction and the residual of the raw image and the reconstructed background is then defined as the salient region(s). Differently, [4] designs conditional variational auto-encoder (CVAE) to model the subjective nature of saliency, where the latent variable is used to model the prediction variants. GAN-based methods can be divided into two categories, namely fully-supervised and semi-supervised settings. The former [102], [103] uses the discriminator to distinguish model predictions from ground truth, while the latter [104], [105] rely on the GAN to explore the contributions of unlabeled data. [106] introduces an inferential Wasserstein GAN model, which is a principled framework to fuse auto-encoders and Wasserstein GAN and jointly learns an encoder network and a generator network motivated by the iterative primal-dual optimization process. Differently, we infer the latent variable via Langevin dynamics [37], which suffers no posterior collapse issue [107].

Weakly Supervised Segmentation Models: Instead of label-consuming pixel-wise annotations, Weakly Supervised Segmentation (WSS) models are designed to explore the possibility of using

weak labels, *e.g.*, image tags [108]–[112], bounding box [113]–[117], scribble [6], [118]–[120], point [121], [122], as supervision. The typical methods [114], [118], [123] usually consider the initial segmentation map produced by traditional unsupervised methods, such as MCG [124] and GrabCut [125], as the supervision to train the deep neural networks and then repeat the iterative process between refinement of the prediction and training of the network. However, the framework tends to introduce accumulated label noise in each step and the iteration is time-consuming. Zhang *et al.* [9] proposed an end-to-end deep learning framework to predict the latent saliency map from multiple noisy saliency maps created by unsupervised handcrafted saliency methods and mitigated the influence of label noise by a specifically-designed noise modeling module. The idea is further extended [126] to use a generative model [38] to model the label noise from a single noisy saliency map. In addition to noise modeling strategies, some methods refine the segmentation map with structure-aware loss functions. Yu *et al.* [120] used partial cross-entropy loss to expand the scribble region to the whole object region and refine the segmentation with a local saliency coherency loss. Most WSS methods are based on CNNs. We explore the potential of transformers for weakly supervised segmentation, especially weakly supervised SOD with scribble supervision [6], [120].

3 ACCURATE AND RELIABLE SALIENT OBJECT DETECTION VIA GENERATIVE TRANSFORMER

As a context-based task, SOD strongly relies on both local and global context, where the former is necessary for identifying median size salient foreground, and the latter is essential for large salient object detection. As discussed in Sec. 1, conventional CNN backbone-based frameworks [2], [30] are effective in modeling the local context, and their performance deteriorates for salient objects that expand to a larger region (see Fig. 1). The self-attention model within the transformer framework [32] enables it to achieve long-range dependency modeling with global context exploration, which is desirable for accurate salient object detection.

Let’s define our training dataset as $D = \{x_i, y_i\}_{i=1}^N$ of size N , where x_i and y_i are the input RGB image (or RGB-D image pair for RGB-D saliency detection) and the corresponding ground truth saliency map, and i indexes the samples, which is omitted. With the transformer backbone (we use θ to represent its parameters), given any testing sample x^* with ground truth y^* , we define its joint distribution as $p(x^*, y^*, \theta|D) = p(y^*|x^*, \theta)p(\theta|D)p(x^*|D)$, where $p(y^*|x^*, \theta)$ represents the predictive distribution or the inherent randomness given θ as the oracle [39], $p(\theta|D)$ explains the ambiguity of the model θ given the provided training dataset D , and $p(x^*|D)$ measures the discrepancy between x^* and the training dataset D .

With the global context modeling ability of transformer, the $p(\theta|D)$ term can be modeled more effectively compared with the CNN frameworks. However, there exists no solution in the transformer framework to model the predictive distribution $p(y^*|x^*, \theta)$. Further, the training/testing discrepancy is not mentioned either, thus it is inconvenient to evaluate the domain gap caused by $p(x^*|D)$. To fix the above-mentioned issues, we introduce a latent variable model with an extra latent variable z involved to model the inherent data noise. Further, we find one of the main domain gap for RGB-D saliency detection lies in the inconsistent depth data as shown in Table 1 and Fig. 2.

We then introduce an auxiliary depth module, achieving self-supervised learning, with which it’s more convenient to evaluate the training/testing discrepancy. Specifically, with extra latent variable z , the joint distribution of the testing sample x^* can be rewritten as:

$$\begin{aligned} & p(x^*, y^*, \theta, z|D) \\ &= \frac{p(x^*, y^*, \theta, z, D)}{p(D)} \\ &= \frac{p(y^*|x^*, \theta, z)p(x^*|\theta, z, D)p(\theta, z, D)}{p(D)} \\ &= p(y^*|x^*, \theta, z)p(\theta|D)p(z|x^*, D)p(x^*|D). \end{aligned} \tag{1}$$

The extra latent variable in Eq. (1) makes it convenient to estimate $p(y^*|x^*, \theta, z)$, where the latent variable z can be sampled from $p(z|x^*, D)$ during testing, modeling the discrepancy between training and testing sample. Specifically, for RGB-D saliency detection, the $p(x^*|D)$ term is modeled directly following self-supervised learning with an auxiliary depth module, which can also be explained as an auto-encoder framework. In the following, we will first introduce a transformer for accurate saliency detection (Sec. 3.1) for effective model parameter estimation ($p(\theta|D)$). We present the auxiliary depth module in Sec. 3.2, achieving an auto-encoder framework to evaluate the domain gap between training and testing samples, or the $p(x^*|D)$ term. We will introduce the latent variable model in Sec. 3.3 to achieve modeling of $p(z|x^*, D)$, with which it’s convenient to model the inherent randomness of model prediction $p(y^*|x^*, \theta, z)$. We present the objective function in Sec. 3.4.

3.1 Transformer for Accurate Saliency Detection

The straightforward solution of using a transformer is to replace the CNN backbone with a transformer backbone, leading to the “transformer encoder”. We take the Swin transformer [34] as our transformer encoder, which takes the embedded image features as input and produces a list of feature maps $f_{\theta_1}(x) = \{t_l\}_{l=1}^4$ of channel size 128, 256, 512 and 1024 respectively, representing different levels of features. Different from [33], [41] that use fixed tokenization, the Swin transformer [34] is a hierarchical transformer structure whose representation is computed with self-attention in shifted non-overlapped windows, thus it enables even larger receptive field modeling. Given the “transformer encoder”, we design a simple “convolution decoder” to achieve high/low level feature aggregation. Specifically, we first feed each backbone feature t_l to a simple convolutional block and obtain the new backbone feature $\{t'_l\}_{l=1}^4$ of the same channel size $C = 32$. Such channel reduction operation aims to further enhance context modeling and reduce the huge memory requirement. Our final saliency map $s = f_{\theta_2}(\{t'_l\}_{l=1}^4)$ is then obtained via a decoder parameterized by θ_2 .

The detailed structure of the decoder can be formulated as $s = f_{\theta_{\text{msd}}}(f_{\theta_{\text{rcab}}}(\{t'_l\}_{l=1}^4))$, where $[\cdot]$ denotes the channel-wise concatenation operation, $f_{\theta_{\text{rcab}}}$ is the residual channel attention block [127], $f_{\theta_{\text{msd}}}$ is the multi-scale dilated convolutional block [128] to obtain a one-channel saliency map. Note that, $\theta = \{\theta_1, \theta_2\}$ indicates the entire parameters of our salient object detection network. $f_{\theta}(x)$ can directly produce the saliency map for RGB image x . For RGB-D saliency detection, we perform early fusion by simply concatenating the RGB image and depth data at the input layer, and feeding it to a 3×3 convolutional layer

to generate a new input tensor x' with a channel size of 3, which is then fed to the saliency generator θ . With the global context modeling ability, the regression ability of the transformer is proven better than CNN frameworks, leading to better θ estimation given the same training dataset D with less ambiguity/uncertainty.

3.2 Auxiliary Depth Module

As we discussed before, the inconsistent depth data (see both Table 1 and Fig. 2) may hinder the performance of existing RGB-D saliency detection models. We then propose an auxiliary depth module to solve the ‘‘distribution gap’’ issue within existing RGB-D SOD datasets. The auxiliary depth module with parameters θ_3 has the same structure as our saliency decoder θ_2 , which takes the backbone feature $f_{\theta_1}(x')$ as input, and outputs a one-channel depth map $d' = f_{\theta_3}(f_{\theta_1}(x'))$. Within this framework, the final loss function has extra depth related loss:

$$\mathcal{L}_{\text{depth}} = \alpha(\beta * \mathcal{L}_{\text{ssim}} + (1 - \beta) * \mathcal{L}_1), \quad (2)$$

where $\alpha = 0.1$ is used to control the contribution of the auxiliary depth module, and following the conventional setting, we set $\beta = 0.85$ in this paper. $\mathcal{L}_{\text{ssim}}$ is the SSIM loss function [129] and \mathcal{L}_1 denotes the L1 loss.

The Auto-encoder for joint distribution modeling: Given a test sample x^* , for a segmentation model with parameters θ , the output distribution is defined as $p(y^*|x^*, \theta)$, and there is no way to model the marginal data distribution $p(x^*)$. For RGB saliency detection, the ‘‘domain gap’’ issue is not that significant. However, for RGB-D saliency detection, we observe differences between training depth data and testing depth data (see Table 1 and Fig. 2), making reliable $p(x^*)$ estimation necessary for RGB-D saliency detection to take into account the training/testing discrepancy. In our setting, with the auxiliary depth module, we obtain the modeling of $p(x^*)$ or $p(x^*|D)$ via conditional self-supervised learning, where the RGB image is the conditional variable. Combining with the main task, *i.e.* salient object detection, we achieve the joint distribution modeling instead of the conditional distribution modeling. The hybrid model [40] is proven more robust to the depth distribution gap issue as discussed in Sec. 1.

3.3 Generative Model for Reliable Saliency Detection

As deep neural networks can fit any random noise [35], the deterministic CNN and transformer backbone based models have serious over-confidence issues, where the model could inaccurately assign a high probability to the wrong prediction. To overcome this, a model which is aware of its prediction with reasonable predictive distribution modeling is desired. As discussed in Eq. (1), a latent variable model makes it convenient to estimate predictive distribution $p(y^*|x^*, \theta, z)$, which can be defined as being Gaussian distribution via:

$$p(y^*|x^*, \theta, z) = \mathcal{N}(\mu(x^*, \theta, z), \sigma^2(x^*, \theta, z)), \quad (3)$$

where the mean is $\mu(x^*, \theta, z) = \mathbb{E}_{z \sim p(z|x^*, D)} p(y^*|x^*, \theta, z)$ and the variance (uncertainty) is $\sigma^2(x^*, \theta, z) = \mathbb{E}_{z \sim p(z|x^*, D)} (p(y^*|x^*, \theta, z) - \mu(x^*, \theta, z))^2$. Eq. (3) presents a convenient solution for evaluating uncertainty from a latent variable model, where the randomness or uncertainty of model prediction is controlled by the latent variable z , making

meaningful z quite desirable for reliable uncertainty estimation. We will first introduce the existing latent variable models and adapt them to our task. We then analyze their advantages and limitations. Based on this, we present the proposed inferential generative adversarial net.

Conventional latent variable models

1) *Generative Adversarial Nets (GAN) [36]:* Within the GAN-based framework, we design an extra fully convolutional discriminator g_β following [105], where β is the parameter set of the discriminator. Two different modules (the saliency generator f_θ and the discriminator g_β in our case) play the minimax game in GAN based framework:

$$\min_{f_\theta} \max_{g_\beta} V(g_\beta, f_\theta) = E_{(x,y) \sim p_{\text{data}}(x,y)} [\log g_\beta(y|x)] + E_{z \sim p(z)} [\log(1 - g_\beta(f_\theta(x, z)))], \quad (4)$$

where $p_{\text{data}}(x, y)$ is the joint distribution of training data, $p(z)$ is the prior distribution of the latent variable z , which is usually defined as $p(z) = \mathcal{N}(0, \mathbf{I})$.

In practice, we define the loss function for the generator as the sum of a reconstruction loss \mathcal{L}_{rec} , and an adversarial loss \mathcal{L}_{adv} , which is $\mathcal{L}_{\text{gen}} = \mathcal{L}_{\text{rec}} + \lambda \mathcal{L}_{\text{adv}}$, where the hyper-parameter λ is tuned, and empirically we set $\lambda = 0.1$ for stable training. For SOD, we define the reconstruction loss \mathcal{L}_{rec} as the structure-aware loss as in Eq. (10), and the adversarial loss as cross-entropy loss: $\mathcal{L}_{\text{adv}} = \mathcal{L}_{\text{ce}}(g_\beta(f_\theta(x, z)), \mathbf{1})$, which fools the discriminator that the prediction is real, where \mathcal{L}_{ce} is the binary cross-entropy loss, and $\mathbf{1}$ is an all-one matrix. The discriminator g_β is trained via the loss function: $\mathcal{L}_{\text{dis}} = \mathcal{L}_{\text{ce}}(g_\beta(f_\theta(x, z)), \mathbf{0}) + \mathcal{L}_{\text{ce}}(g_\beta(y), \mathbf{1})$, which aims to correctly distinguish prediction and ground truth. Similarly, $\mathbf{0}$ is an all-zero matrix. In this way, the generator loss and the discriminator loss can be summarized as:

$$\begin{aligned} \mathcal{L}_{\text{gen}} &= \mathcal{L}_{\text{rec}} + \lambda \mathcal{L}_{\text{adv}}, \\ \mathcal{L}_{\text{dis}} &= \mathcal{L}_{\text{ce}}(g_\beta(f_\theta(x, z)), \mathbf{0}) + \mathcal{L}_{\text{ce}}(g_\beta(y), \mathbf{1}). \end{aligned} \quad (5)$$

2) *Variational Auto-encoder (VAE) [96]:* For dense prediction task with input variable x and output variable y , we refer to conditional variational auto-encoder (CVAE) [98] instead, where the input image x is the conditional variable. As a conditional directed graph model, a conventional CVAE mainly contains two modules: a generator model $f_\theta(x)$, which is a saliency generator in this paper, to produce the task related predictions, and an inference model $q_\theta(z|x, y)$, which infers the latent variable z with image x and annotation y as input. Learning a CVAE framework involves approximation of the true posterior distribution of z with an inference model $q_\theta(z|x, y)$, with the loss function as:

$$\begin{aligned} \mathcal{L}_{\text{cvae}} &= \underbrace{\mathbb{E}_{h \sim q_\theta(z|x,y)} [-\log p_\theta(y|x, z)]}_{\mathcal{L}_{\text{rec}}} \\ &+ D_{KL}(q_\theta(z|x, y) \parallel p_\theta(z|x)). \end{aligned} \quad (6)$$

The first term is the reconstruction loss and the second is the Kullback-Leibler divergence of prior distribution $p_\theta(z|x)$ and posterior distribution $q_\theta(z|x, y)$, where both of them are usually parameterized by multi-layer perceptron (MLP).

3) *Alternating back-propagation (ABP):* Alternating back-propagation [38] updates the latent variable and network parameters in an EM manner. Given the network prediction with the current parameter set, it infers the latent variable by the Langevin dynamics based Markov Chain Monte Carlo (MCMC) [37], which is called ‘‘Inferential back-propagation’’ [38]. Given the updated

3. we define x^* as RGB image for RGB saliency detection and RGB-D image pair for RGB-D saliency detection.

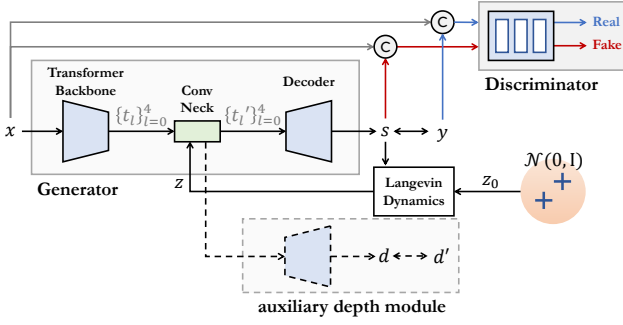


Fig. 3. Flowchart of our proposed inferential GAN (iGAN) (note that the “auxiliary depth” module is removed for RGB SOD). The “Generator” takes image x and latent variable z as input, and generates saliency map s , where the latent variable z is updated via the Langevin dynamics based MCMC [37]. The fully convolutional “Discriminator” is designed to distinguish prediction (fake) and ground truth (real). d' is the predicted depth for RGB-D SOD.

latent variable z , the network parameter set is updated with gradient descent, which is called “Learning back-propagation” [38]. Similar to the VAE [96] or CVAE [98] frameworks, ABP intends to infer z and learn the network parameter θ to minimize the reconstruction loss. Specifically, ABP [38] samples z directly from its posterior distribution with a gradient-based Monte Carlo method, namely Langevin Dynamics [37]:

$$z_{t+1} = z_t + \frac{s_t^2}{2} \left[\frac{\partial}{\partial z} \log p_\theta(y, z_t | x) \right] + s_t \mathcal{N}(0, \mathbf{I}), \quad (7)$$

where $z_0 \sim \mathcal{N}(0, \mathbf{I})$, and the gradient term is defined as:

$$\frac{\partial}{\partial z} \log p_\theta(y, z | x) = \frac{1}{\sigma^2} (y - f_\theta(x, z)) \frac{\partial}{\partial z} f_\theta(x, z) - z. \quad (8)$$

t is the time step for Langevin sampling, s_t is the step size, σ^2 is variance of the inherent labeling noise. As no extra network is involved in the ABP based framework, the final loss function contains only the task-related loss.

Analysis of the conventional latent variable models: As no inference model is included in GAN [36], the latent variable z within GAN is always sampled from the standard normal distribution $\mathcal{N}(0, \mathbf{I})$, which is less informative. For the CVAE based model [96], [98], it samples the latent variable z from the designed posterior distribution during training, and the distribution gap between the designed posterior and the true distribution leads to the posterior collapse issue [107], where the latent variable is independent of the input image, leading to less representative latent space. For the ABP [38] based framework, although it samples from the true posterior distribution via Eq. (7), the task related training is not changed, and our experimental results show that the deterministic performance is usually heavily influenced, especially for the conventional CNN backbone based frameworks.

The proposed inferential GAN

For the VAE [96], [98] based framework, as parameters of the reconstruction model and the posterior net, are updated together, the convergence of the D_{KL} term in Eq. (6) may influence the convergence of the reconstruction part, which is also discussed in [130]. Although beta-VAE [130] can slightly balance the convergence of the two parts, carefully picked hyper-parameters are needed. For the ABP [38] based framework, the basic assumption to achieve sampling from the true posterior distribution is that the

time step should be large enough, and the step size should be infinitely small (see Eq. (8)). For the GAN [36] based framework, the less informative latent space makes it not ideal to be directly used to model the predictive distribution. However, its adversarial training strategy can usually lead to better model performance than the other two latent variable models. In this paper, we introduce inferential generative adversarial network (iGAN), a new generative model for SOD, where we infer the latent variable within the proposed framework instead of defining it as fixed $\mathcal{N}(0, \mathbf{I})$. Specifically, the proposed iGAN infers the latent variable by gradient-based Markov Chain Monte Carlo (MCMC), namely Langevin dynamics [37] (see Fig. 3) following ABP [38], leading to an image conditioned latent variable. Further, as adversarial training is applied, our new generative model can achieve reliable latent space exploration with fewer time steps.

Algorithm 1 iGAN for fully supervised salient object detection

Input: (1) Training images $\{x_i\}_1^N$ with associated saliency maps $\{y_i\}_1^N$, where i indexes images, and N is the size of the training dataset (We perform early fusion for RGB-D saliency detection model). (2) Maximal number of learning epochs Ep ; (3) Numbers of Langevin steps for posterior T ; (4) Langevin step sizes for posterior s_t and variance of inherent labeling noise σ^2 .

Output: Parameters θ for the generator and β for the discriminator.

- 1: Initialize θ and β
- 2: **for** $ep \leftarrow 1$ to Ep **do**
- 3: Sample image-saliency pairs $\{(x_i, y_i)\}_i^N$
- 4: For each (x_i, y_i) , sample the prior $z_0^i \sim \mathcal{N}(0, \mathbf{I})$, and sample the posterior z_t^i using T Langevin steps in Eq. (7) with a step size s_t and inherent noise σ^2 .
- 5: Update the transformer generator with model prediction $f_\theta(x, z_t^i)$ using the generator loss function in Eq. (5).
- 6: Update the discriminator with loss function in Eq. (9).
- 7: **end for**

Following the previous variable definitions, given the training example (x, y) , we intend to infer z and learn the network parameters θ to minimize the reconstruction loss as well as a regularization term that corresponds to the prior on z . Our iGAN based framework includes three main parts: a generator for task related predictions, a discriminator to distinguish the prediction and ground truth, and an inference model via Langevin dynamics [37] to infer the latent variable with gradient based MCMC. Different from the isotropic Gaussian distribution assumption for the latent variable in GAN [36], or the possible posterior issue [107] within VAE [96], our latent variable z is sampled directly from its real posterior distribution via gradient based MCMC following [38]. Further, we introduce extra adversarial loss and the fully convolutional discriminator, serving as a higher-order loss function for accurate deterministic predictions. Empirically, we set $s_t = 0.1$ and $\sigma^2 = 0.3$ in Eq. (7) and Eq. (8). During training, we sample z_0 from $\mathcal{N}(0, \mathbf{I})$, and update z via Eq. (7) by running $T = 5$ steps of Langevin sampling [37], and the final z_T is then used to generate saliency prediction in our case. For testing, we can sample directly from the prior distribution $\mathcal{N}(0, \mathbf{I})$.

Network Details: The proposed iGAN can be applied to any deterministic saliency detection model, and we show the flowchart of the proposed iGAN for saliency detection in Fig. 3. Specifically, we first extend the latent variable z to the same spatial size as the highest level backbone feature (t_4 in this paper). Then we concatenate z with t_4 channel-wise and feed it to a 3×3 convolutional layer, which will serve as the new t_4 for saliency prediction. The discriminator contains four 3×3 convolutional

layers following batch normalization and leakyReLU activation function with 64 channels, which takes the concatenation of image and model prediction (or ground truth) as input to estimate its pixel-wise realism. In this way, the discriminator loss in Eq. (5) can be rewritten as:

$$\mathcal{L}_{\text{dis}} = \mathcal{L}_{\text{ce}}(g_{\beta}([f_{\theta}(x, z), x]), \mathbf{0}) + \mathcal{L}_{\text{ce}}(g_{\beta}([y, x]), \mathbf{1}), \quad (9)$$

where $[\cdot, \cdot]$ is the channel-wise concatenation operation. The training of the proposed iGAN is the same as the conventional GAN based models in Eq. (5), except that we have an extra inference model via MCMC [37]. We show the learning pipeline of iGAN in Algorithm 1.

Inferential GAN analysis: Same as other generative models, iGAN aims to produce reliable uncertainty maps while keeping the deterministic performance unchanged. As the conventional GAN [36] has no inference step, the latent variable is independent of the input image x , leading to less informative uncertainty maps while sampling from the latent space at test time. Although VAE [96] and ABP [38] can produce input-dependent latent space modeling, the possible posterior collapse [107] issue within the former and the less accurate deterministic prediction of the latter limit their applications for SOD. With the proposed iGAN, we can achieve two main benefits: 1) extra inference step is included without increasing model parameters, leading to an input-dependent latent variable; 2) with the adversarial loss function serving as a high-order similarity measure, iGAN can lead to more effective model learning compared with ABP [38]. For the former, our iGAN is built upon GAN [36] and ABP [38], and the fully convolutional discriminator introduces less than 1M extra parameters, which is comparable to both the alternative latent variable models and the deterministic models. For the latter, the adversarial training is proven effective in maintaining the deterministic performance compared with the alternative stochastic models.

3.4 Objective Function

For RGB saliency detection, we remove the ‘‘auxiliary depth’’ module from Fig. 3. The objective is shown in Eq. (5), where the reconstruction loss \mathcal{L}_{rec} is chosen as the structure-aware loss from [3], which is the sum of the weighted binary cross-entropy loss and the weighted IOU loss:

$$\mathcal{L}_{\text{rec}}^{\text{RGB}} = \omega(\mathcal{L}_{\text{ce}}(s, y) + \mathcal{L}_{\text{iou}}(s, y)), \quad (10)$$

where y is the ground truth saliency map, ω is the edge-aware weight, and is defined as $\omega = 1 + 5 * |(ap(y) - y)|$, with $ap(\cdot)$ representing the average pooling operation. \mathcal{L}_{ce} is the binary cross-entropy loss. \mathcal{L}_{iou} is the weighted IOU loss [3].

For RGB-D saliency detection, Fig. 3 represents the entire training pipeline. As shown, we introduce an auxiliary depth module to model the joint distribution in Eq. (1). Specifically, as an early fusion model, we concatenate the RGB image and depth data at the input level, which is then fed to a 3×3 convolutional layer to produce a tensor with channel size 3, which is defined as the fused input x' . The proposed iGAN framework for RGB-D SOD takes x' as input and produces both saliency map s and depth prediction d' . The reconstruction loss for RGB-D saliency detection is defined as:

$$\mathcal{L}_{\text{rec}}^{\text{RGBD}} = \omega(\mathcal{L}_{\text{ce}}(s, y) + \mathcal{L}_{\text{iou}}(s, y)) + \lambda \mathcal{L}_{\text{depth}}, \quad (11)$$

where λ is used to balance the contribution of the auxiliary depth module, and empirically we set $\lambda = 1$. The generator loss and

discriminator loss are obtained following Eq. (5). Note that for both RGB and RGB-D SOD models, the latent variable z is updated via Langevin dynamics as shown in Eq. (7).

4 EXPERIMENTS

Dataset: In this paper, we conduct research on salient object detection (SOD), including both RGB image-based SOD and RGB-D image pair-based SOD. For the former, we perform fully and weakly supervised saliency detection. Within the fully supervised learning frameworks, we train the models by using the DUTS training dataset [7] $D1 = \{x_i, y_i\}_{i=1}^N$ of size $N = 10,553$, and test on six other widely used datasets: the DUTS testing dataset, ECSSD [131], DUT [132], HKU-IS [133], PASCAL-S [134] and the SOD testing dataset [135]. For the weakly supervised models, we use the DUTS-S training dataset [6], $D2 = \{x_i, y_i\}_{i=1}^N$ of size $N = 10,553$, where y_i is the scribble annotation. The testing dataset is the same as the fully supervised RGB SOD models.

For RGB-D SOD, we follow the conventional setting, where the training set $D3 = \{x_i, y_i\}_{i=1}^N$ is a combination of 1,485 images from the NJU2K dataset [24] and 700 images from the NLPR dataset [21]. We then test the performance of our model and competing models on the NJU2K testing set, NLPR testing set, LFS [26], DES [23], SSB [19] and SIP [28] dataset.

Evaluation Metrics: For all three tasks, we use four evaluation metrics to measure the performance, including Mean Absolute Error \mathcal{M} , Mean F-measure (F_{β}), Mean E-measure ($E_{\mathcal{E}}$) [139] and S-measure (S_{α}) [140].

MAE \mathcal{M} is defined as the pixel-wise difference between the prediction s and the ground truth y : $\mathcal{M} = \frac{1}{H \times W} |c - y|$, where H and W are the height and width of c correspondingly.

F-measure F_{β} is a region-based similarity metric, and we provide the mean F-measure using varying fixed (0-255) thresholds.

E-measure $E_{\mathcal{E}}$ is the recently proposed Enhanced alignment measure [139] in the binary map evaluation field to jointly capture image-level statistics and local pixel matching information.

S-measure S_{α} is a structure based measure [140], which combines the region-aware (S_r) and object-aware (S_o) structural similarity as their final structure metric: $S_{\alpha} = \alpha S_o + (1 - \alpha) S_r$, where $\alpha \in [0, 1]$ is set to 0.5 by default.

Calibration measures: Due to the close correlation between uncertainty estimation and model calibration [35], uncertainty is usually evaluated with modal calibration measures [141], *i.e.* expected calibration error (ECE) [142]. The basic assumption is that a reliable uncertainty output should lead to a well-calibrated model, where model confidence is consistent with model accuracy.

4.1 Accurate and Reliable Fully-supervised Salient Object Detection

4.1.1 Performance Comparison with Benchmark Models

We compare the proposed framework with benchmark saliency models and show model performance in Tables 2, 3 and 4. Note that, VST [94] and GTSOD [95] are two existing transformer based saliency detection models.

We observe the competitive performance of our CNN based generative model (CIGAN) with existing techniques in Tables 2 and 3. To focus on explaining the superior performance of the transformer backbone for SOD, our decoder has only 1M parameters, which is around 5% of model parameters of existing techniques. Further, we find a better performance of our generative

TABLE 2
Performance comparison with benchmark fully-supervised RGB SOD models.

Method	DUTS [7]				ECSSD [131]				DUT [132]				HKU-IS [133]				PASCAL-S [134]				SOD [135]			
	$S_{\alpha} \uparrow$	$F_{\beta} \uparrow$	$E_{\xi} \uparrow$	$\mathcal{M} \downarrow$	$S_{\alpha} \uparrow$	$F_{\beta} \uparrow$	$E_{\xi} \uparrow$	$\mathcal{M} \downarrow$	$S_{\alpha} \uparrow$	$F_{\beta} \uparrow$	$E_{\xi} \uparrow$	$\mathcal{M} \downarrow$	$S_{\alpha} \uparrow$	$F_{\beta} \uparrow$	$E_{\xi} \uparrow$	$\mathcal{M} \downarrow$	$S_{\alpha} \uparrow$	$F_{\beta} \uparrow$	$E_{\xi} \uparrow$	$\mathcal{M} \downarrow$	$S_{\alpha} \uparrow$	$F_{\beta} \uparrow$	$E_{\xi} \uparrow$	$\mathcal{M} \downarrow$
CIGAN	.876	.820	.906	.042	.923	.913	.945	.037	.823	.733	.848	.061	.911	.892	.943	.034	.856	.836	.893	.068	.833	.816	.862	.075
TIGAN	.909	.873	.941	.028	.941	.936	.964	.025	.861	.796	.890	.047	.929	.918	.962	.025	.879	.869	.916	.054	.861	.854	.894	.060
SCRN [2]	.885	.833	.900	.040	.920	.910	.933	.041	.837	.749	.847	.056	.916	.894	.935	.034	.869	.833	.892	.063	.817	.790	.829	.087
F3Net [3]	.888	.852	.920	.035	.919	.921	.943	.036	.839	.766	.864	.053	.917	.910	.952	.028	.861	.835	.898	.062	.824	.814	.850	.077
ITSD [136]	.886	.841	.917	.039	.920	.916	.943	.037	.842	.767	.867	.056	.921	.906	.950	.030	.860	.830	.894	.066	.836	.829	.867	.076
PAKRN [12]	.900	.876	.935	.033	.928	.930	.951	.032	.853	.796	.888	.050	.923	.919	.955	.028	.859	.856	.898	.068	.833	.836	.866	.074
MSFNet [61]	.877	.855	.927	.034	.915	.927	.951	.033	.832	.772	.873	.050	.909	.913	.957	.027	.849	.855	.900	.064	.813	.822	.852	.077
CTDNet [137]	.893	.862	.928	.034	.925	.928	.950	.032	.844	.779	.874	.052	.919	.915	.954	.028	.861	.856	.901	.064	.829	.832	.858	.074
VST [94]	.896	.842	.918	.037	.932	.911	.943	.034	.850	.771	.869	.058	.928	.903	.950	.030	.873	.832	.900	.067	.854	.833	.879	.065
GTSOD [95]	<u>.908</u>	<u>.875</u>	.942	<u>.029</u>	<u>.935</u>	<u>.935</u>	<u>.962</u>	<u>.026</u>	<u>.858</u>	.797	.892	.051	.930	.922	.964	.023	<u>.877</u>	.855	<u>.915</u>	.054	<u>.860</u>	.860	.898	<u>.061</u>

TABLE 3
Performance comparison with benchmark fully-supervised RGB-D SOD models.

Method	NJU2K [24]				SSB [19]				DES [23]				NLPR [21]				LFSD [26]				SIP [28]			
	$S_{\alpha} \uparrow$	$F_{\beta} \uparrow$	$E_{\xi} \uparrow$	$\mathcal{M} \downarrow$	$S_{\alpha} \uparrow$	$F_{\beta} \uparrow$	$E_{\xi} \uparrow$	$\mathcal{M} \downarrow$	$S_{\alpha} \uparrow$	$F_{\beta} \uparrow$	$E_{\xi} \uparrow$	$\mathcal{M} \downarrow$	$S_{\alpha} \uparrow$	$F_{\beta} \uparrow$	$E_{\xi} \uparrow$	$\mathcal{M} \downarrow$	$S_{\alpha} \uparrow$	$F_{\beta} \uparrow$	$E_{\xi} \uparrow$	$\mathcal{M} \downarrow$	$S_{\alpha} \uparrow$	$F_{\beta} \uparrow$	$E_{\xi} \uparrow$	$\mathcal{M} \downarrow$
CIGAN	.914	.900	.939	.036	.903	.876	.934	.040	.937	.921	.970	.018	.922	.890	.952	.025	.851	.832	.889	.075	.884	.870	.917	.049
TIGAN	<u>.928</u>	<u>.919</u>	.956	.028	<u>.915</u>	<u>.893</u>	<u>.947</u>	<u>.034</u>	<u>.940</u>	.929	.970	.016	<u>.932</u>	<u>.911</u>	<u>.961</u>	<u>.020</u>	.884	<u>.862</u>	<u>.911</u>	.057	<u>.905</u>	<u>.901</u>	.941	.037
BBSNet [5]	.921	.902	.938	.035	.908	.883	.928	.041	.933	.910	.949	.021	.930	.896	.950	.023	.864	.843	.883	.072	.879	.868	.906	.055
BiaNet [76]	.915	.903	.934	.039	.904	.879	.926	.043	.931	.910	.948	.021	.925	.894	.948	.024	.845	.834	.871	.085	.883	.873	.913	.052
CoNet [74]	.911	.903	<u>.944</u>	.036	.896	.877	.939	.040	.906	.880	.939	.026	.900	.859	.937	.030	.842	.834	.886	.077	.868	.855	.915	.054
UCNet [4]	.897	.886	.930	.043	.903	.884	.938	.039	.934	.919	.967	.019	.920	.891	.951	.025	.864	.855	.901	.066	.875	.867	.914	.051
JLDCF [16]	.902	.885	.935	.041	.903	.873	.936	.040	.931	.907	.959	.021	.925	.894	.955	.022	.862	.848	.894	.070	.880	.873	.918	.049
VST [94]	.922	.898	.939	.035	.913	.879	.937	.038	<u>.943</u>	.920	<u>.965</u>	<u>.017</u>	<u>.932</u>	.897	.951	.024	<u>.882</u>	.871	.917	<u>.061</u>	.904	.894	.933	<u>.040</u>
GTSOD [95]	.929	.924	.956	.028	.916	.898	.950	.032	.945	<u>.928</u>	.971	.016	.938	.921	.966	.018	.872	.862	.901	.066	.906	.908	<u>.940</u>	.037

TABLE 4
Performance comparison with benchmark weakly-supervised RGB SOD models.

Method	DUTS [7]				ECSSD [131]				DUT [132]				HKU-IS [133]				PASCAL-S [134]				SOD [135]			
	$S_{\alpha} \uparrow$	$F_{\beta} \uparrow$	$E_{\xi} \uparrow$	$\mathcal{M} \downarrow$	$S_{\alpha} \uparrow$	$F_{\beta} \uparrow$	$E_{\xi} \uparrow$	$\mathcal{M} \downarrow$	$S_{\alpha} \uparrow$	$F_{\beta} \uparrow$	$E_{\xi} \uparrow$	$\mathcal{M} \downarrow$	$S_{\alpha} \uparrow$	$F_{\beta} \uparrow$	$E_{\xi} \uparrow$	$\mathcal{M} \downarrow$	$S_{\alpha} \uparrow$	$F_{\beta} \uparrow$	$E_{\xi} \uparrow$	$\mathcal{M} \downarrow$	$S_{\alpha} \uparrow$	$F_{\beta} \uparrow$	$E_{\xi} \uparrow$	$\mathcal{M} \downarrow$
CIGAN	.834	.779	.887	.056	.896	.890	.938	.044	.799	.713	.838	.070	.886	.873	.938	.039	.827	.810	.880	.079	.800	.793	.855	.083
TIGAN	.855	<u>.814</u>	.918	.043	.905	.905	.950	.037	.826	.760	.874	.058	.893	<u>.887</u>	.949	.035	.844	.839	.902	.066	.811	.810	.872	.082
SSAL [6]	.803	.747	.865	.062	.863	.865	.908	.061	.785	.702	.835	.068	.865	.858	.923	.047	.798	.773	.854	.093	.750	.743	.801	.108
WSS [7]	.748	.633	.806	.100	.808	.774	.801	.106	.730	.590	.729	.110	.822	.773	.819	.079	.701	.691	.687	.187	.698	.635	.687	.152
C2S [138]	.805	.718	.845	.071	-	-	-	-	.773	.665	.810	.082	.869	.837	.910	.053	.784	.806	.813	.130	.770	.741	.799	.117
SCWS [120]	<u>.841</u>	.818	<u>.901</u>	<u>.049</u>	.879	.894	.924	.051	<u>.813</u>	<u>.751</u>	<u>.856</u>	<u>.060</u>	.883	.892	<u>.938</u>	<u>.038</u>	.821	<u>.815</u>	.877	<u>.078</u>	.782	.791	.833	.090

model (TIGAN) compared with VST [94], indicating the superiority of the proposed model. Different from the deterministic VST [94], as a generative model, we aim to produce stochastic predictions leading to reliable saliency prediction. In this way, we compare with GTSOD [95], another generative transformer SOD model, in the way of both accurate and reliable saliency prediction. Tables 2 and 3 show that the proposed iGAN achieves comparable performance compared with GTSOD [95], leading to an alternative generative saliency transformer. In Fig. 4, we further visualize the produced uncertainty maps of GTSOD [95] and ours for RGB SOD. The more reliable uncertainty maps, highlighting the less confident or hard regions, further explain our superiority. Besides the visual comparison, we also compute calibration measures of GTSOD [95] and ours and show the results in Table 6, which clearly shows the advantages of our model in achieving better calibrated models compared with GTSOD [95].

4.1.2 Accurate Saliency Model

In Sec. 1, we discuss that the CNN backbone is not effective in detecting salient objects that rely on global context and the stride and pooling operation lead to less accurate structure information of CNN backbone features. We then compare the performance of CNN backbone (B_cnn with ResNet50 [18] backbone) and

transformer backbone model (B_tr with Swin transformer backbone [34]) for RGB image based SOD, and show performance in Table 5, where the models share the same decoder⁴. Note that, for both B_cnn and B_tr, we use binary cross-entropy loss for the saliency generator. To further explain how the two types of backbone based models perform with structure-aware loss [3] in Eq. (10), we train B_cnn and B_tr with a structure-aware loss instead and obtain model B'_cnn and B'_tr respectively. We also visualize predictions from the two different backbone networks in Fig. 5. The significant performance gap between the two different backbones (B_cnn and B_tr) indicates the superiority of the transformer backbone for SOD. Further, we observe, although the transformer has encoded accurate structure information, the structure-aware loss function (B'_tr) that penalizes the wrong prediction along object boundaries can lead to more accurate predictions (see Table 5 and Fig. 5).

Transformer backbone for large salient object detection:

As discussed, the larger receptive field of transformer backbone makes it ideal for the context based task, *i.e.* salient object detection. We then visualize the performance (we use mean absolute error (MAE) here as it's easy to implement and share the similar performance comparison trend with other measures) of CNN

4. We adjust the decoder accordingly to the backbone features.

TABLE 5

Baseline model performance, where B_cnn and B_tr are models with CNN and transformer backbones respectively using a binary cross-entropy loss function, B'_cnn and B'_tr are the corresponding models with the structure-aware loss function in Eq. (10).

Method	DUTS [7]				ECSSD [131]				DUT [132]				HKU-IS [133]				PASCAL-S [134]				SOD [135]			
	$S_\alpha \uparrow$	$F_\beta \uparrow$	$E_\xi \uparrow$	$\mathcal{M} \downarrow$	$S_\alpha \uparrow$	$F_\beta \uparrow$	$E_\xi \uparrow$	$\mathcal{M} \downarrow$	$S_\alpha \uparrow$	$F_\beta \uparrow$	$E_\xi \uparrow$	$\mathcal{M} \downarrow$	$S_\alpha \uparrow$	$F_\beta \uparrow$	$E_\xi \uparrow$	$\mathcal{M} \downarrow$	$S_\alpha \uparrow$	$F_\beta \uparrow$	$E_\xi \uparrow$	$\mathcal{M} \downarrow$	$S_\alpha \uparrow$	$F_\beta \uparrow$	$E_\xi \uparrow$	$\mathcal{M} \downarrow$
B_cnn	.878	.818	.895	.042	.922	.907	.937	.039	.822	.724	.834	.061	.912	.886	.933	.035	.862	.838	.891	.067	.831	.808	.846	.079
B'_cnn	.882	.840	.916	.037	.922	.919	.947	.035	.823	.742	.851	.057	.912	.901	.947	.030	.855	.841	.896	.065	.832	.825	.863	.073
B_tr	.907	.863	.930	.031	.939	.929	.957	.028	.858	.786	.878	.051	.929	.912	.954	.027	.881	.866	.911	.056	.854	.841	.882	.065
B'_tr	.911	.882	.947	.026	.939	.940	.965	.024	.860	.801	.894	.045	.927	.921	.964	.023	.876	.872	.917	.053	.858	.853	.897	.059

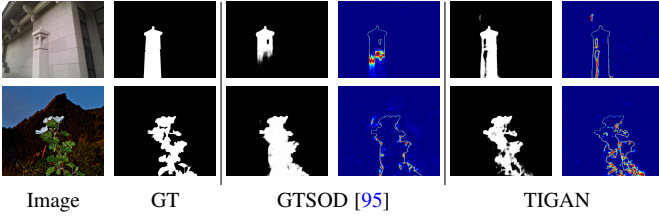


Fig. 4. Performance comparison with existing generative SOD model GTSOD [95], where prediction in each block is the model prediction and the corresponding uncertainty map.

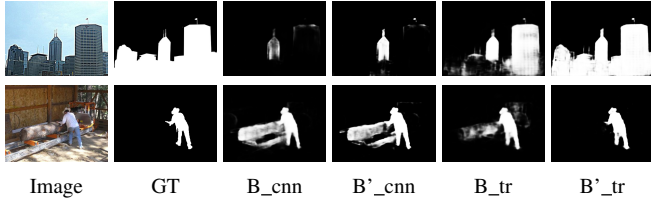


Fig. 5. Predictions of CNN and transformer backbone models without (B_cnn and B_tr) and with (B'_cnn and B'_tr) structure-aware loss.

TABLE 6

Calibration degree of conventional uncertainty estimation techniques and the proposed inferential GAN with transformer backbone.

	DUTS	ECSSD	DUT	HKU-IS	PASCAL-S	SOD
	[7]	[131]	[132]	[133]	[134]	[135]
GTSOD [95]	.0388	.0214	.0461	.0231	.0476	.0552
MCD	.0391	.0230	.0468	.0234	.0498	.0581
TGAN	.0382	.0227	.0464	.0227	.0488	.0570
TCVAE	.0377	.0220	.0441	.0229	.0497	.0560
TABP	.0365	.0204	.0430	.0211	.0487	.0545
TIGAN	.0353	.0198	.0400	.0198	.0467	.0519

backbone (B'_cnn) and transformer backbone (B'_tr) w.r.t. size of the salient foreground in Fig. 6. Specifically, we uniformly group the scale of salient foreground to 10 bins and compute the mean performance of each backbone based model. Fig. 6 shows that the transformer backbone based model outperforms the CNN backbone based model almost consistently across all scales. Specifically, the performance gap for the largest foreground scale (on the DUT [132] and SOD datasets [135]) is the most significant compared with other scales, which explains the superiority of the transformer for large salient object detection. There also exist scales for the HKU-IS [133] and PASCAL-S [134] datasets when the transformer backbone based model fails to outperform the CNN backbone based model, which are mainly due to the “double-edged sword” effect of the transformer’s larger receptive field, which will be explained in Sec. 4.3. Images in ECSSD dataset [131] are relatively simpler compared with other datasets,

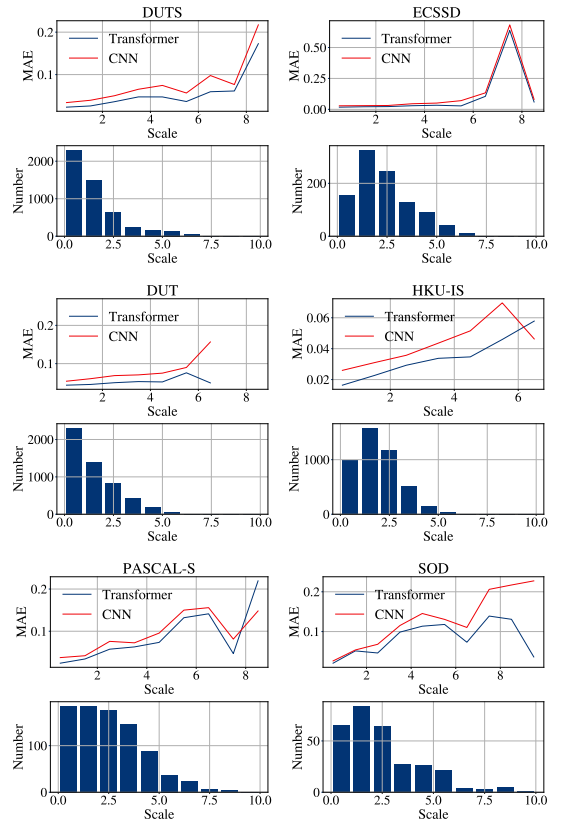


Fig. 6. Model (B'_cnn and B'_tr in Table 5) performance (the top curve of each block) w.r.t. salient foreground size distribution (the bottom bar of each block) on six testing datasets.

and the foreground objects are distributed compactly around the image center, leading to less significant performance gain with the transformer backbone.

Auxiliary depth module for depth domain gap modeling: We discuss this in Sec. 1 that the inconsistent depth distribution (see Table 1 and Fig. 2) leads to a domain gap between the training datasets and testing datasets for RGB-D salient object detection. To solve the issue, we present an auxiliary depth module to fully explore the depth contribution and fix the depth domain gap via self-supervised learning. To evaluate the effectiveness of the proposed auxiliary depth module, we design three SOD models, namely the pure RGB image based model (“CB_RGB” and “TB_RGB”), early fusion model (“CEarly” and “TEarly”) and early fusion model with auxiliary depth module (“CADE” and “TADE”), where “C*” represents CNN backbone (ResNet50 [18]), and “T*” is the transformer backbone. The performance of each model is shown in Table 7.

Firstly, we observe the improved performance of early fusion

TABLE 7

Depth contribution analysis for RGB-D SOD. Given the RGB image based model (“*_RGB”), we first adapt it for RGB-D saliency detection with early-fusion (“*_Early”). Then, the auxiliary depth module is attached to “*_Early” to analyze the depth contribution.

Method	NJU2K [24]				SSB [19]				DES [23]				NLPR [21]				LFSD [26]				SIP [28]			
	$S_\alpha \uparrow$	$F_\beta \uparrow$	$E_\xi \uparrow$	$\mathcal{M} \downarrow$	$S_\alpha \uparrow$	$F_\beta \uparrow$	$E_\xi \uparrow$	$\mathcal{M} \downarrow$	$S_\alpha \uparrow$	$F_\beta \uparrow$	$E_\xi \uparrow$	$\mathcal{M} \downarrow$	$S_\alpha \uparrow$	$F_\beta \uparrow$	$E_\xi \uparrow$	$\mathcal{M} \downarrow$	$S_\alpha \uparrow$	$F_\beta \uparrow$	$E_\xi \uparrow$	$\mathcal{M} \downarrow$	$S_\alpha \uparrow$	$F_\beta \uparrow$	$E_\xi \uparrow$	$\mathcal{M} \downarrow$
CB_RGB	.906	.891	.936	.038	.903	.882	.933	.039	.908	.890	.936	.025	.916	.891	.948	.025	.802	.777	.833	.105	.874	.862	.913	.052
CEarly	.912	.901	.941	.036	.903	.881	.934	.038	.932	.921	.964	.018	.914	.886	.945	.026	.830	.804	.858	.082	.878	.864	.914	.050
CADE	.911	.902	.939	.036	.902	.877	.936	.039	.935	.922	.968	.018	.922	.896	.951	.025	.860	.848	.899	.069	.888	.880	.925	.045
TB_RGB	.924	.919	.955	.029	.922	.906	.952	.030	.918	.908	.943	.022	.931	.914	.962	.021	.869	.856	.899	.067	.895	.898	.935	.042
TEarly	.925	.917	.955	.028	.911	.890	.948	.033	.938	.926	.974	.016	.935	.916	.865	.019	.875	.862	.903	.060	.897	.895	.938	.039
TADE	.925	.917	.953	.029	.911	.890	.946	.034	.944	.930	.977	.015	.934	.913	.965	.018	.879	.869	.910	.056	.902	.895	.939	.038

TABLE 8

Reliable fully-supervised RGB SOD models, where we present performance of stochastic saliency prediction models via GAN, CVAE, ABP as well as the proposed iGAN. Performance of the baseline deterministic models (B*_cnn and B*_tr in Table 5) are listed for easier reference.

Method	DUTS [7]				ECSSD [131]				DUT [132]				HKU-IS [133]				PASCAL-S [134]				SOD [135]			
	$S_\alpha \uparrow$	$F_\beta \uparrow$	$E_\xi \uparrow$	$\mathcal{M} \downarrow$	$S_\alpha \uparrow$	$F_\beta \uparrow$	$E_\xi \uparrow$	$\mathcal{M} \downarrow$	$S_\alpha \uparrow$	$F_\beta \uparrow$	$E_\xi \uparrow$	$\mathcal{M} \downarrow$	$S_\alpha \uparrow$	$F_\beta \uparrow$	$E_\xi \uparrow$	$\mathcal{M} \downarrow$	$S_\alpha \uparrow$	$F_\beta \uparrow$	$E_\xi \uparrow$	$\mathcal{M} \downarrow$	$S_\alpha \uparrow$	$F_\beta \uparrow$	$E_\xi \uparrow$	$\mathcal{M} \downarrow$
CGAN	.881	.839	.917	.036	.919	.916	.945	.036	.818	.734	.845	.056	.909	.898	.945	.031	.857	.845	.899	.064	.818	.807	.846	.078
CCVAE	.877	.833	.911	.040	.922	.920	.949	.034	.817	.735	.845	.063	.910	.900	.947	.031	.855	.842	.897	.066	.830	.822	.866	.073
CABP	.828	.757	.859	.058	.887	.877	.913	.055	.778	.670	.801	.078	.878	.855	.913	.047	.810	.782	.845	.094	.773	.744	.799	.102
CIGAN	.876	.820	.906	.042	.923	.913	.945	.037	.823	.733	.848	.061	.911	.892	.943	.034	.856	.836	.893	.068	.833	.816	.862	.075
B*_cnn	.882	.840	.916	.037	.922	.919	.947	.035	.823	.742	.851	.057	.912	.901	.947	.030	.855	.841	.896	.065	.832	.825	.863	.073
TGAN	.907	.877	.944	.029	.939	.938	.964	.025	.852	.789	.882	.051	.927	.920	.963	.024	.878	.872	.918	.053	.855	.849	.894	.061
TCVAE	.908	.879	.945	.028	.940	.940	.966	.024	.857	.796	.890	.048	.927	.922	.964	.024	.876	.871	.918	.054	.858	.854	.898	.060
TABP	.910	.878	.944	.028	.942	.940	.966	.024	.860	.799	.891	.048	.929	.922	.964	.024	.879	.870	.918	.054	.860	.858	.897	.061
TIGAN	.909	.873	.941	.028	.941	.936	.964	.025	.861	.796	.890	.047	.929	.918	.962	.025	.879	.869	.916	.054	.861	.854	.894	.060
B*_tr	.911	.882	.947	.026	.939	.940	.965	.024	.860	.801	.894	.045	.927	.921	.964	.023	.876	.872	.917	.053	.858	.853	.897	.059

TABLE 9

Reliable fully-supervised RGB-D SOD models, where we present performance of stochastic saliency prediction models via GAN, CVAE, ABP as well as the proposed iGAN. Performance of the baseline models (CADE and TADE in Table 7) are listed for easier reference.

Method	NJU2K [24]				SSB [19]				DES [23]				NLPR [21]				LFSD [26]				SIP [28]			
	$S_\alpha \uparrow$	$F_\beta \uparrow$	$E_\xi \uparrow$	$\mathcal{M} \downarrow$	$S_\alpha \uparrow$	$F_\beta \uparrow$	$E_\xi \uparrow$	$\mathcal{M} \downarrow$	$S_\alpha \uparrow$	$F_\beta \uparrow$	$E_\xi \uparrow$	$\mathcal{M} \downarrow$	$S_\alpha \uparrow$	$F_\beta \uparrow$	$E_\xi \uparrow$	$\mathcal{M} \downarrow$	$S_\alpha \uparrow$	$F_\beta \uparrow$	$E_\xi \uparrow$	$\mathcal{M} \downarrow$	$S_\alpha \uparrow$	$F_\beta \uparrow$	$E_\xi \uparrow$	$\mathcal{M} \downarrow$
CGAN	.914	.905	.943	.035	.904	.881	.937	.039	.929	.917	.957	.019	.924	.899	.954	.023	.849	.826	.884	.074	.885	.875	.921	.047
CCVAE	.906	.894	.937	.039	.896	.871	.934	.041	.940	.923	.975	.017	.916	.891	.951	.026	.841	.825	.881	.075	.887	.878	.927	.045
CABP	.916	.903	.941	.034	.905	.878	.935	.039	.941	.928	.972	.017	.921	.891	.949	.025	.845	.828	.876	.077	.888	.876	.922	.046
CIGAN	.914	.900	.939	.036	.903	.876	.934	.040	.937	.921	.970	.018	.922	.890	.952	.025	.851	.832	.889	.075	.884	.870	.917	.049
CADE	.911	.902	.939	.036	.902	.877	.936	.039	.935	.922	.968	.018	.922	.896	.951	.025	.860	.848	.899	.069	.888	.880	.925	.045
TGAN	.928	.921	.956	.027	.911	.890	.946	.034	.941	.931	.975	.015	.934	.915	.964	.019	.875	.860	.903	.060	.900	.901	.939	.038
TCVAE	.928	.922	.956	.028	.911	.889	.944	.035	.941	.929	.973	.016	.935	.915	.964	.020	.879	.863	.905	.060	.903	.904	.941	.038
TABP	.927	.917	.954	.029	.913	.891	.947	.034	.943	.929	.974	.015	.933	.911	.962	.020	.870	.852	.900	.065	.904	.900	.942	.037
TIGAN	.928	.919	.956	.028	.915	.893	.947	.034	.940	.929	.970	.016	.932	.911	.961	.020	.884	.868	.911	.057	.905	.901	.941	.037
TADE	.925	.917	.953	.029	.911	.890	.946	.034	.944	.930	.977	.015	.934	.913	.965	.018	.879	.869	.910	.056	.902	.895	.939	.038

models compared with training only with RGB images, indicating the benefits of depth for SOD. Further, as shown in Fig. 2, salient foreground depth contrast of the LFSD dataset [26] is most different from the corresponding RGB image salient foreground contrast. In this way, we claim that the auxiliary depth module should contribute the most, which is consistent with our experiments. Note that, the proposed auxiliary depth module aims to further explore the depth contribution, especially for depth data that distributes differently from the training dataset.

4.1.3 Reliable Saliency Model

Model reliability is an important factor for measuring accountability for decisions before deployment, and a reliable model should be aware of its predictions. In this paper, we introduce the iGAN for reliable saliency detection with an image conditioned latent prior. In addition to the proposed iGAN, we also design GAN-based [36], CVAE-based [96], [98] and ABP-based [38] generative models for RGB SOD and RGB-D SOD. The performance is shown in Table 8 and Table 9 respectively, where “CGAN”, “CCVAE”, “CABP” and “CIGAN” are the stochastic

models based on GAN, CVAE, ABP, and the proposed inferential GAN respectively with CNN backbone, and “TGAN”, “TCVAE”, “TABP” and “TIGAN” are the transformer counterparts.

For easier reference, we also include the baseline models B*_cnn and B*_tr from Table 5 in Table 8, and the CNN and transformer backbone based stochastic models are built upon the two baseline models respectively. The stochastic RGB-D SOD models in Table 9 are based on the corresponding RGB-D SOD models with auxiliary depth module as shown in Table 7. We show the performance of “CADE” and “TADE” for easier reference. Table 8 and Table 9 show that the four types of generative models can achieve comparable deterministic performance (compared with the corresponding deterministic baseline models) for both RGB image based SOD and RGB-D image pair based SOD. As the goal of a generative model is to obtain stochastic predictions for the model explanation, the deterministic performance may be slightly lower. The proposed inferential GAN, e.g. “CABP” for RGB SOD. The main reason lies in two parts. First, the hyper-parameters within the inference model in Eq. (7) need to be tuned to effectively explore the latent space. Second, the final performances of those

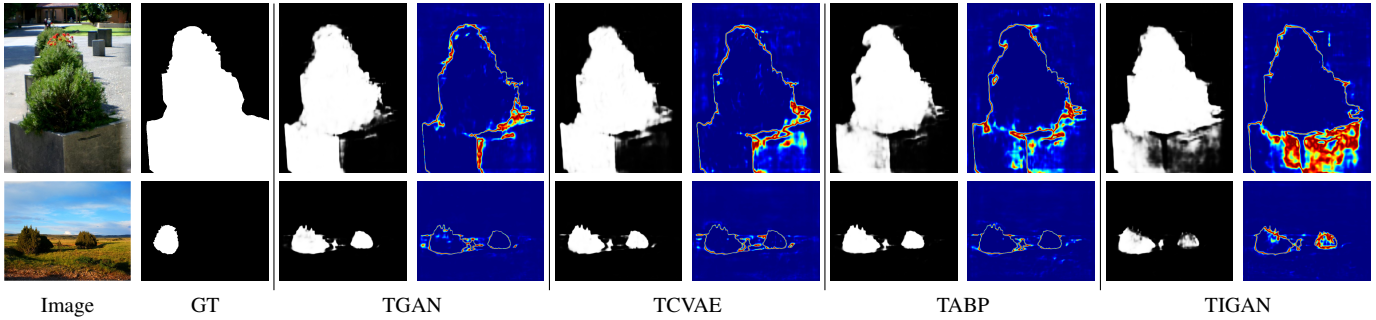


Fig. 7. Predictions from different generative models in Table 8, where we randomly sample $T = 10$ times and obtain the entropy of mean prediction as predictive uncertainty [39]. Note that the predictions within each method block are saliency prediction and uncertainty respectively.

TABLE 10

Weakly-supervised SOD models analysis with both the CNN and transformer backbone, where models in the top block are the CNN based models with different weakly supervised loss functions, and models in the bottom block are the corresponding transformer based counterparts.

Method	DUTS [7]				ECSSD [131]				DUT [132]				HKU-IS [133]				PASCAL-S [134]				SOD [135]			
	$S_\alpha \uparrow$	$F_\beta \uparrow$	$E_\xi \uparrow$	$\mathcal{M} \downarrow$	$S_\alpha \uparrow$	$F_\beta \uparrow$	$E_\xi \uparrow$	$\mathcal{M} \downarrow$	$S_\alpha \uparrow$	$F_\beta \uparrow$	$E_\xi \uparrow$	$\mathcal{M} \downarrow$	$S_\alpha \uparrow$	$F_\beta \uparrow$	$E_\xi \uparrow$	$\mathcal{M} \downarrow$	$S_\alpha \uparrow$	$F_\beta \uparrow$	$E_\xi \uparrow$	$\mathcal{M} \downarrow$	$S_\alpha \uparrow$	$F_\beta \uparrow$	$E_\xi \uparrow$	$\mathcal{M} \downarrow$
BCNN	.754	.641	.806	.088	.822	.771	.868	.087	.723	.588	.758	.107	.807	.739	.864	.080	.760	.703	.812	.117	.745	.692	.801	.117
BCNN_S	.805	.724	.858	.069	.869	.846	.913	.060	.771	.664	.806	.088	.859	.822	.913	.055	.802	.768	.855	.095	.780	.750	.841	.098
BCNN_G	.835	.781	.884	.053	.895	.889	.934	.046	.796	.708	.831	.068	.883	.871	.932	.041	.825	.807	.874	.080	.797	.787	.843	.870
BCNN_self	.787	.682	.834	.077	.851	.803	.888	.075	.761	.634	.793	.089	.833	.767	.880	.072	.796	.743	.839	.100	.766	.716	.811	.111
BCNN_weak	.839	.792	.892	.050	.895	.892	.934	.044	.800	.719	.835	.063	.886	.877	.935	.039	.829	.813	.880	.078	.788	.778	.834	.088
BT	.748	.636	.798	.081	.834	.786	.885	.071	.728	.600	.765	.099	.802	.734	.861	.077	.777	.727	.830	.100	.756	.710	.820	.108
BT_S	.829	.767	.893	.053	.886	.878	.938	.045	.807	.726	.854	.069	.869	.848	.932	.046	.825	.810	.884	.078	.802	.791	.869	.085
BT_G	.857	.808	.916	.043	.908	.903	.951	.036	.825	.751	.870	.059	.896	.883	.949	.035	.843	.831	.898	.069	.819	.813	.877	.077
BT_self	.791	.683	.840	.070	.854	.799	.893	.069	.773	.649	.809	.083	.832	.763	.882	.070	.802	.748	.846	.094	.781	.732	.836	.101
BT_weak	.858	.815	.917	.042	.908	.907	.952	.035	.835	.770	.879	.054	.898	.891	.952	.034	.848	.843	.904	.065	.821	.819	.880	.075

generative models are obtained by performing multiple iterations (10 iterations in this paper) of forward passes during testing, and the performance of the mean prediction is then reported, which varies with different iterations of sampling. In this paper, we focus on the new generative model for accurate and reliable SOD, we leave the generative model hyper-parameter tuning for future work.

Besides the deterministic performance, the main advantage of the generative model is its ability for stochastic predictions, making it possible to estimate predictive uncertainty [39] for model reliability estimation. In Fig. 7, we visualize the uncertainty maps of each generative model. In this paper, the ‘‘uncertainty’’ refers to predictive uncertainty [39], [143], which is the total uncertainty, including both data uncertainty and model uncertainty. Given the mean predictions after multiple forward passes during testing, the predictive uncertainty is defined as the entropy of the mean prediction. A reliable model should be aware of its prediction, leading to a reasonable uncertainty model to explain model prediction. Fig. 7 shows that the uncertainty map from the proposed inferential GAN explains better model prediction, highlighting the hard samples caused by training/testing discrepancy. Especially, for the 1st sample the bottom region is relatively low-contrast, which is different from the high-contrast foreground in the training dataset. The ground truth of the 2nd image is biased, focusing only on a compact foreground region, where the less compact region is discarded. All four latent variable models can discover the discarded less compact region, where the uncertainty map of ‘‘TIGAN’’ is more informative in explaining the less accurate predictions (see Table 6 for extensive comparison).

4.2 Accurate and Reliable Weakly-supervised Salient Object Detection

Different from pixel-wise annotation based fully supervised SOD, weakly supervised SOD models learn saliency from cheap annotations, e.g., scribble annotations [6], image-level labels [7]. In this paper, we investigate the superiority of the transformer backbone for weakly supervised SOD with scribble supervision [6].

4.2.1 Weakly-supervised Transformer

The main difficulty of learning from weak annotations is the missing structure information, which cannot be recovered without extra structure-aware regularizers. In this way, the main focus of designing models to learn from weak annotations is to recover the missing structure information. Specifically, we investigate three widely used strategies, namely smoothness loss [144], gated CRF loss [123], and data-augmentation based consistency loss. The first and second ones aim to recover the structure of prediction, and the third one aims to achieve transformation robust prediction, serving as an internal data augmentation trick. To test how the model performs with different loss functions within both the CNN framework and the transformer framework, we design models with each type of loss function within both the CNN backbone and transformer backbone and report the performance in Table 10.

Implementation details: To train the weakly-supervised transformer for SOD, similar to [6], we adopt extra smoothness loss [144] \mathcal{L}_{sm} , the gated CRF loss [123] \mathcal{L}_{gcrf} and the data-augmentation based self-supervised learning strategy [120] \mathcal{L}_{ss} to recover the missing structure information in scribble annotation. The smoothness loss aims to produce a saliency map with edges well-aligned with the input image. The gated CRF loss introduces pairwise constraints to produce a saliency map with spatial consistency. The self-supervised learning strategy

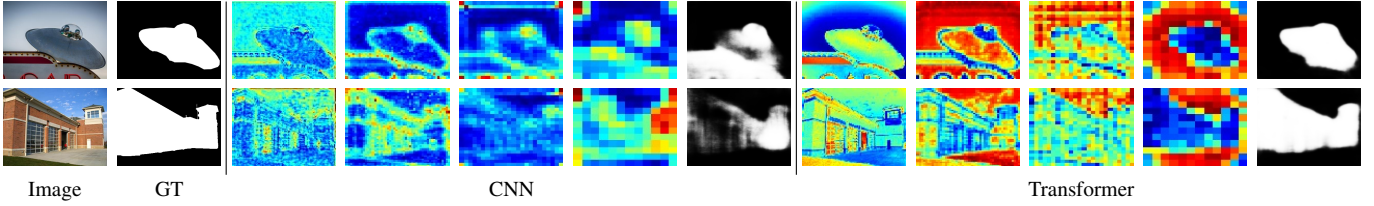


Fig. 8. Features of CNN (ResNet50 [18]) and transformer backbone (Swin [34]) for weakly-supervised SOD using only partial cross-entropy loss.

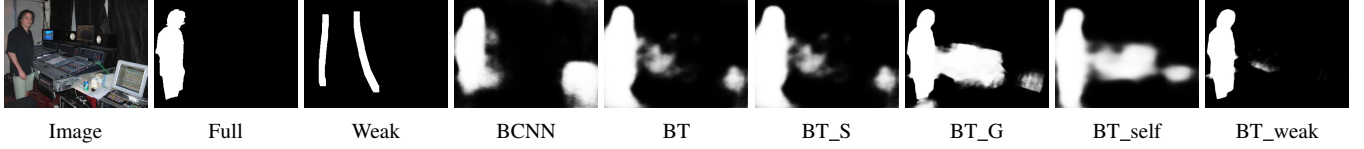


Fig. 9. Weakly supervised saliency model predictions with different loss functions. Detailed performance of each model is illustrated in Table 10.

aims to achieve transformation robust predictions. For the Swin transformer backbone [34], as it can only take fixed-size input, we perform image rotation instead of image scaling to achieve data augmentation. Specifically, we define the self-supervised loss as a weighted sum of the structural similarity measure [129] and L_1 loss, which is defined as:

$$\mathcal{L}_{ss} = \alpha * SSIM(s, s^t) + (1 - \alpha) * \mathcal{L}_1(s, s^t), \quad (12)$$

where $s = f_\theta(T(x))$ is the output of the generator with the rotated image⁵ $T(x)$ as input, and $s^t = T(f_\theta(x))$ is the rotated prediction with original image x as input. We randomly pick the rotation $T(\cdot)$ from $\{\pi, 1/2\pi, -1/2\pi\}$ in our experiments. α is used to balance the two types of loss functions and we set $\alpha = 0.85$ in our experiments following [120]. Further, given the scribble annotation, we adopt the partial cross-entropy loss \mathcal{L}_{pce} to constrain predictions on the scribble region. In this way, we define the loss function for the weakly-supervised model as:

$$\mathcal{L}_{weak} = \mathcal{L}_{pce} + \lambda_1 * \mathcal{L}_{sm} + \lambda_2 * \mathcal{L}_{gcrf} + \lambda_3 * \mathcal{L}_{ss}. \quad (13)$$

With grid search, we set $\lambda_1 = 0.3$, $\lambda_2 = 1.0$ and $\lambda_3 = 1.2$.

CNN backbone vs Transformer backbone: We design two different models with ResNet50 [18] and Swin transformer [34] as the backbone. The decoder part is the same as B’_tr in Table 5. We train the two models with only partial cross-entropy loss, and we show their corresponding results in Table 10 “BCNN” and “BT” respectively. The significantly improved performance of “BT” compared with “BCNN” shows the effectiveness of the transformer backbone for weakly-supervised SOD. We also visualize the features of the two trained models in Fig. 8, where heat maps are the features and gray maps are the predictions. We observe clear structure information in “Transformer”, which explains the superior performance of the transformer for weakly-supervised learning via supervisions with less structure information [145].

Weakly-supervised loss analysis: Besides the partial cross-entropy loss, we use three extra loss functions for weakly-supervised SOD, namely smoothness loss to constrain the predictions to be well aligned with the image edges, gated CRF loss to regularize the pairwise term predictions which aim to produce similar predictions for spatially similar pixels, and a self-supervised loss to effectively learn from less supervision data with

consistency loss, *e.g.*, rotation-invariant predictions. We then carry out extra experiments to verify the effectiveness of each loss function and show the results in Table 10. “BCNN_S”, “BCNN_G” and “BCNN_self” indicate baseline model (“BCNN”) training with extra smoothness loss “ \mathcal{L}_{sm} ”, gated CRF loss “ \mathcal{L}_{gcrf} ” and self-supervised loss “ \mathcal{L}_{ss} ”. “BT_S”, “BT_G” and “BT_self” are the corresponding transformer backbone counterparts. We observe an improved performance of each extra loss function, which explains their effectiveness. Further, we find that the smoothness and gated CRF achieve more performance gain than the self-supervised loss, which mainly comes from their effective structure modeling ability. The improved performance of BCNN_weak and BT_weak with the weighted loss function in Eq. (13) compared with the corresponding models with individual loss functions verifies the effectiveness of the proposed weighted weakly supervised loss function. We also show predictions of the weakly supervised models in Fig. 9. It is clear that both the base model with only partial cross-entropy loss (“BCNN” and “BT”) and the model with extra self-supervised loss (“BT_self”) fail to accurately localize object boundaries, leading to blurred predictions. The main reason is the absence of structure constraints. The smoothness loss and the gated CRF loss work better in modeling the structure information, leading to more accurate predictions, especially along object boundaries, and models (“BCNN_weak” and “BT_weak”) with our final loss function (Eq. (13)) achieve the best performance.

4.2.2 Reliable Weakly-supervised Transformer

The generative models for the fully-supervised setting are straightforward, as we can simply take the inferred latent variable as part of the input, and the discriminator can directly estimate the real/fake of its input (the ground truth/model prediction). In this section, we apply our proposed inferential GAN (iGAN) to weakly-supervised RGB SOD. We also design the GAN [36], CVAE [96], [98], and ABP [38] based generative models for comparison. Similarly, we design the generative model within both the CNN backbone and the transformer backbone. The performance is shown in Table 11, where “CGAN”, “CCVAE”, “CABP” and “CIGAN” are the stochastic models based on GAN, CVAE, ABP, and the proposed inferential GAN respectively with CNN backbone, and “TGAN”, “TCVAE”, “TABP” and “TIGAN” are the corresponding transformer counterparts. Same as the fully-supervised reliable models in Table 8 and Table 9, the prior

5. In this paper, we perform image rotation instead of image scaling due to the fixed input size of Swin transformer [34].

TABLE 11
Reliable weakly-supervised RGB SOD models, where the deterministic models (“*_weak”) is trained loss function in Eq. (13).

Method	DUTS [7]				ECSSD [131]				DUT [132]				HKU-IS [133]				PASCAL-S [134]				SOD [135]			
	$S_\alpha \uparrow$	$F_\beta \uparrow$	$E_\xi \uparrow$	$\mathcal{M} \downarrow$	$S_\alpha \uparrow$	$F_\beta \uparrow$	$E_\xi \uparrow$	$\mathcal{M} \downarrow$	$S_\alpha \uparrow$	$F_\beta \uparrow$	$E_\xi \uparrow$	$\mathcal{M} \downarrow$	$S_\alpha \uparrow$	$F_\beta \uparrow$	$E_\xi \uparrow$	$\mathcal{M} \downarrow$	$S_\alpha \uparrow$	$F_\beta \uparrow$	$E_\xi \uparrow$	$\mathcal{M} \downarrow$	$S_\alpha \uparrow$	$F_\beta \uparrow$	$E_\xi \uparrow$	$\mathcal{M} \downarrow$
CGAN	.834	.785	.887	.053	.891	.888	.932	.046	.792	.706	.826	.069	.881	.873	.933	.041	.828	.814	.880	.079	.798	.797	.852	.082
CCVAE	.832	.781	.882	.055	.894	.889	.934	.045	.793	.708	.827	.070	.883	.872	.933	.041	.822	.806	.876	.081	.797	.792	.851	.085
CABP	.838	.790	.893	.051	.894	.890	.935	.044	.801	.718	.838	.064	.887	.878	.937	.039	.828	.813	.882	.078	.794	.791	.848	.084
CIGAN	.834	.779	.887	.056	.896	.890	.938	.044	.799	.713	.838	.070	.886	.873	.938	.039	.827	.810	.880	.079	.800	.793	.855	.083
BCNN_weak	.839	.792	.892	.050	.895	.892	.934	.044	.800	.719	.835	.063	.886	.877	.935	.039	.829	.813	.880	.078	.788	.778	.834	.088
TGAN	.856	.813	.918	<u>.043</u>	.906	.905	.950	.037	.824	.753	.868	.060	<u>.895</u>	.886	.949	<u>.035</u>	.848	.840	<u>.905</u>	<u>.065</u>	<u>.819</u>	<u>.816</u>	<u>.878</u>	<u>.076</u>
TCVAE	.855	.813	.916	<u>.043</u>	<u>.907</u>	<u>.906</u>	.950	<u>.036</u>	.825	.757	.872	.059	.894	<u>.887</u>	.949	<u>.035</u>	.843	.837	.900	.067	.814	.813	.873	.079
TABP	.854	.812	<u>.917</u>	<u>.043</u>	.905	.905	<u>.951</u>	<u>.036</u>	<u>.827</u>	<u>.759</u>	<u>.875</u>	<u>.058</u>	.893	<u>.887</u>	<u>.950</u>	<u>.035</u>	<u>.847</u>	.844	.906	.064	.810	.810	.868	.082
TIGAN	.855	.814	.918	<u>.043</u>	.905	.905	.950	.037	.826	<u>.760</u>	.874	<u>.058</u>	.893	<u>.887</u>	.949	<u>.035</u>	.844	.839	.902	.066	.811	.810	.872	.082
BT_weak	.858	.815	<u>.917</u>	.042	.908	.907	.952	.035	.835	.770	.879	.054	.898	.891	.952	.034	.848	<u>.843</u>	.904	<u>.065</u>	.821	.819	.880	.075

TABLE 12
Model analysis related experiments, where we discuss model performance with respect to model optimizer (“B’_SGD” and “B’_trSGD”), initialization weights (“B’_R”, B’_trR and B’_tr22K) and different transformer backbones (“B’_ViT”).

Method	DUTS [7]				ECSSD [131]				DUT [132]				HKU-IS [133]				PASCAL-S [134]				SOD [135]			
	$S_\alpha \uparrow$	$F_\beta \uparrow$	$E_\xi \uparrow$	$\mathcal{M} \downarrow$	$S_\alpha \uparrow$	$F_\beta \uparrow$	$E_\xi \uparrow$	$\mathcal{M} \downarrow$	$S_\alpha \uparrow$	$F_\beta \uparrow$	$E_\xi \uparrow$	$\mathcal{M} \downarrow$	$S_\alpha \uparrow$	$F_\beta \uparrow$	$E_\xi \uparrow$	$\mathcal{M} \downarrow$	$S_\alpha \uparrow$	$F_\beta \uparrow$	$E_\xi \uparrow$	$\mathcal{M} \downarrow$	$S_\alpha \uparrow$	$F_\beta \uparrow$	$E_\xi \uparrow$	$\mathcal{M} \downarrow$
B’_cnn	.882	.840	.916	.037	.922	.919	.947	.035	.823	.742	.851	.057	.912	.901	.947	.030	.855	.841	.896	.065	.832	.825	.863	.073
B’_SGD	.876	.826	.910	.041	.918	.910	.944	.038	.820	.733	.846	.062	.909	.894	.945	.033	.856	.840	.895	.067	.827	.813	.863	.077
B’_R	.745	.623	.773	.110	.832	.789	.853	.093	.738	.605	.762	.114	.820	.760	.858	.084	.752	.697	.777	.140	.725	.673	.758	.145
B’_tr	.911	.882	.947	.026	.939	.940	<u>.965</u>	<u>.024</u>	.860	.801	.894	.045	.927	.921	.964	.023	.876	.872	.917	<u>.053</u>	<u>.858</u>	<u>.853</u>	<u>.897</u>	.059
B’_trSGD	.899	.861	.936	.031	.928	.923	.954	.032	.854	.786	.886	.046	.921	.909	.956	.029	.867	.856	.905	.061	.833	.818	.862	.075
B’_trR	.768	.667	.804	.097	.848	.819	.874	.082	.754	.637	.784	.105	.843	.803	.884	.070	.760	.715	.794	.134	.730	.689	.763	.142
B’_tr22K	.918	.891	.952	<u>.025</u>	.944	.943	.967	.022	.869	.814	.902	.044	.933	.928	.968	<u>.022</u>	.885	.881	<u>.925</u>	.050	.863	.863	.900	.059
B’_ViT	.922	.899	.955	.023	<u>.943</u>	<u>.945</u>	.967	.022	.874	.824	.906	.043	.934	.931	.969	.021	<u>.884</u>	.884	.926	.050	<u>.858</u>	<u>.859</u>	.895	.065

TABLE 13
Replacing the CNN backbone of existing RGB SOD models with a transformer backbone.

Method	DUTS [7]				ECSSD [131]				DUT [132]				HKU-IS [133]				PASCAL-S [134]				SOD [135]			
	$S_\alpha \uparrow$	$F_\beta \uparrow$	$E_\xi \uparrow$	$\mathcal{M} \downarrow$	$S_\alpha \uparrow$	$F_\beta \uparrow$	$E_\xi \uparrow$	$\mathcal{M} \downarrow$	$S_\alpha \uparrow$	$F_\beta \uparrow$	$E_\xi \uparrow$	$\mathcal{M} \downarrow$	$S_\alpha \uparrow$	$F_\beta \uparrow$	$E_\xi \uparrow$	$\mathcal{M} \downarrow$	$S_\alpha \uparrow$	$F_\beta \uparrow$	$E_\xi \uparrow$	$\mathcal{M} \downarrow$	$S_\alpha \uparrow$	$F_\beta \uparrow$	$E_\xi \uparrow$	$\mathcal{M} \downarrow$
SCRN [2]	.885	.833	.900	.040	.920	.910	.933	.041	.837	.749	.847	.056	.916	.894	.935	.034	.869	.833	.892	.063	.817	.790	.829	.087
F3Net [3]	.888	.852	.920	.035	.919	.921	.943	.036	.839	.766	.864	.053	.917	.910	.952	.028	.861	.835	.898	.062	.824	.814	.850	.077
SCRN* [2]	.908	.873	.937	.029	<u>.937</u>	.935	<u>.960</u>	.027	.864	.800	.890	<u>.044</u>	.930	.919	<u>.958</u>	<u>.026</u>	<u>.875</u>	<u>.870</u>	.911	.057	.843	.836	.865	.069
F3Net* [3]	.913	.891	.950	.024	.939	.941	.965	.023	<u>.860</u>	.802	<u>.891</u>	.042	<u>.928</u>	.925	.964	.023	.872	.872	<u>.916</u>	<u>.055</u>	<u>.848</u>	<u>.849</u>	<u>.881</u>	<u>.065</u>
B’_tr	<u>.911</u>	<u>.882</u>	<u>.947</u>	<u>.026</u>	.939	<u>.940</u>	.965	<u>.024</u>	<u>.860</u>	<u>.801</u>	.894	.045	.927	.921	.964	.023	.876	.872	.917	.053	.858	.853	.897	.059

and posterior distribution models of the CVAE based models are designed following [4].

Implementation details: For the learning process of the reliable weakly-supervised transformer, we apply the same pipeline of the fully supervised method. Considering there is only scribble ground-truth as supervision in training the discriminator, we use partial cross-entropy loss for training the discriminator within the GAN and our proposed iGAN based models, and the adversarial loss \mathcal{L}_{adv} is also partial cross-entropy loss.

Performance analysis: For easier reference, we also list the baseline models “BCNN_weak” and “BT_weak” from Table 10 and Table 11, and the CNN and transformer backbone based stochastic models are built upon the two baseline models respectively. Same as the results of fully supervised SOD models in Table 8, the three types of generative models for weakly-supervised SOD can also achieve comparable deterministic performance.

4.3 Discussions

We further analyze our transformer backbone-based models in details. Unless otherwise stated, the experiments are based on the fully supervised deterministic RGB SOD (“B’_tr” in Table 5).

Model performance w.r.t. optimizer: We observe that the AdamW optimizer is more suitable to train the transformer backbone (Swin [34] in particular) based framework compared with

SGD. To explain this, we train B’_cnn and B’_tr with SGD as optimizer, leading to B’_SGD and B’_trSGD respectively in Table 12. We observe that for both the CNN and transformer backbone based networks, the SGD optimizer usually achieves worse performance compared with the AdamW optimizer. Note that models with the two types of optimizers share the same initial learning rate, and “SGD” in this paper is SGD with a momentum of 0.9. We find that after the first epoch, the AdamW optimizer based model jumps directly to a minimum of smaller loss compared with SGD, and later, the loss decrease behaviors of both models are similar. We also tried different learning rate configurations for models with the two types of the optimizers, and the performance of SGD based model is still bad. We further explore whether the AdamW converges faster than SGD. However, even when we train more epochs for SGD based model, the conclusion is still similar. We will investigate it further to extensively explain the different model behaviors with various types of optimizers.

The importance of initialization weights: For both CNN and transformer backbone, we initialize them with the image classification model trained on the ImageNet-1K [146] dataset. To test how the initialization weights contribute to the model performance, we randomly initialize the two models (B’_cnn and B’_tr in Table 5) and obtain model performance as B’_R and B’_trR in Table 12. We observe the worse performance of

both B'_R and B'_trR, which further illustrates the necessity of fine-tuning the backbone models for SOD. We also initialize our transformer backbone with parameters pre-trained on the ImageNet-22K dataset and show the result as B'_tr22K in Table 12. The better performance of B'_tr22K compared with B'_tr again explains the importance of the initialization weights.

Different transformer backbones analysis: Following our pipeline, we change the Swin transformer backbone [34] to the ViT backbone [33], [41], and achieve B'_ViT in Table 12. Note that, the ViT backbone we used in Table 12 is initialized with weights trained on ImageNet-22K. The comparable performance of B'_ViT compared with B'_tr22K explains that the two types of backbones both work for SOD.

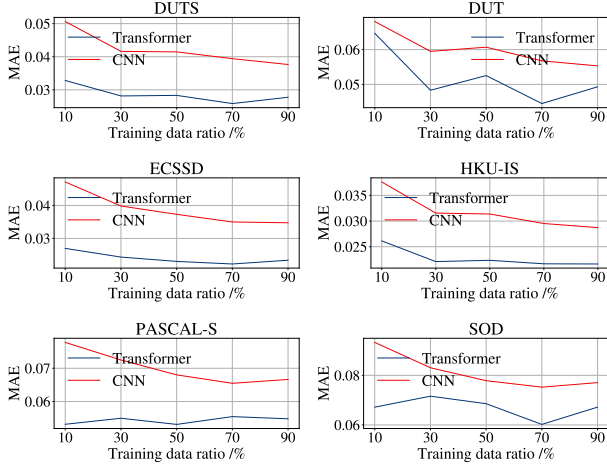


Fig. 10. Model performance of the CNN backbone and the transformer backbone w.r.t. different training dataset sizes on six testing datasets.

Model performance w.r.t. training datasets scales: As the two types of backbones have significantly different numbers of model parameters, leading to different model capacities. We aim to analyze how model capacity is sensitive to scales of the training dataset. We then train our transformer backbone networks (B'_tr) and CNN backbone based model (B'_cnn) in Table 5) with different sizes of training datasets, which are 10%, 30%, 50%, 70%, 90% of the entire training dataset respectively, and report the model performance in Fig. 10. The consistently better performance of the transformer backbone-based model with regard to different numbers of training examples explains its effectiveness. Meanwhile, we observe that the model performance is not always increasing with a larger training dataset, which inspires us to work on an active learning-based transformer network to actively select representative samples for model training.

Model performance with different decoders: To test how the transformer encoder performs with different decoders, we change the backbone of existing SOD models (SCRN [2] and F3Net [3]) to transformer backbone [34], and show their performance in Table 13, where “*” is the transformer backbone based counterpart. Table 13 shows that the transformer backbone can indeed improve the performance of existing SOD models. However, we observe similar performance of model with our decoder (B'_tr) (around 1M parameters) compared with other complicated decoders (more than 20M for both SCRN [2] and F3Net [3]). The Swin backbone model [34] has around 85M parameters, and its high capacity poses challenges to the decoder design. We argue

that the transformer-compatible decoder should be investigated to further explore the contribution of transformer backbones.

Model performance with conventional uncertainty estimation techniques: A systematic way to deal with model uncertainty is via Bayesian statistics [39], [143], [149]–[151]. Bayesian Neural Networks aim to learn a distribution over each of the network parameters by placing a prior probability distribution over network weights, *i.e.* $p(\theta|D)$. According to the Bayesian rule, the posterior over model parameters $p(\theta|x, y)$ (or $p(\theta|D)$) can be achieved as:

$$p(\theta|x, y) = \frac{p(x, y|\theta)p(\theta)}{p(x, y)} = \frac{p(x, y|\theta)p(\theta)}{\int p(x, y|\theta)p(\theta)d\theta}. \quad (14)$$

The marginalization over θ to calculate $p(x, y)$ in the denominator is intractable. $p(\theta|x, y)$ is then not available in closed-form, making it computationally intractable to calculate the exact Bayesian posterior. More efforts have been put into developing approximations of Bayesian Neural Network that can work in practice, including Variational Inference (VI) [152]–[154] and Markov Chain Monte Carlo (MCMC) [155]. [156] shows that a neural network of arbitrary depth and non-linearity, with dropout applied before every weighted layer, is mathematically equivalent to an approximation to the probabilistic deep Gaussian process [157] (GP). Based on it, [156] further shows that the dropout objective minimizes the KL divergence between an approximate distribution and the posterior of a deep Gaussian process. In this paper, we apply MC-dropout [156] as a free-lunch model uncertainty estimation technique to our baseline model B'_tr in Table 8 with dropout rate 0.3, and show its performance in Table 6, which again verify the effectiveness of our model in achieving better model calibration.

Robustness to adversarial attack: Deep neural network based models are known to suffer from adversarial examples. With small perturbations, model predictions can be changed drastically [158]. Common defense methods for adversarial attacks include adversarial training [148], certified robustness [159], *etc.* In this paper, we investigate model robustness with respect to adversarial attack. Specifically, we discuss FGSM [147], a gradient based attack, and perform adversarial training [148] to achieve model defense.

FGSM [147] attack only needs to do backprop once to get the gradient of classification loss with respect to the input x , and the adversarial sample x_{adv} can be generated via:

$$x_{adv} = x + \varepsilon \text{sign}(\nabla_x \mathcal{L}(\theta, x, y)), \quad (15)$$

where $\mathcal{L}(\theta, x, y)$ is the classification loss, and the sign function is used to achieve faster convergence. Correspondingly, the adversarial training based defense is achieved via training the model with adversarial sample pair (x_{adv}, y) , leading to a new objective:

$$\min_{\theta} \mathbb{E}_{(x, y) \sim \mathcal{D}} \left[\max_{\delta \in \mathcal{S}} \mathcal{L}(\theta, x + \delta, y) \right], \quad (16)$$

where \mathcal{S} is the candidate adversarial attacks. In practice, a more efficient way to achieve adversarial training based defense is through joint training with both clean sample x and adversarial sample x_{adv} with weighted loss:

$$\min_{\theta} (\alpha \mathcal{L}(\theta, x, y) + (1 - \alpha) \mathcal{L}(\theta, x_{adv}, y)), \quad (17)$$

where $\alpha = 0.5$ is used to control the balance of accurate prediction ($\mathcal{L}(\theta, x, y)$) and model robustness ($\mathcal{L}(\theta, x_{adv}, y)$).

In this paper, we perform adversarial attack with FGSM [147] and defense with adversarial training in Eq. (17) to both the baseline models (B'_cnn and B'_tr in Table 8) and the proposed iGAN

TABLE 14
Model robustness to adversarial attack and defense.

Method	DUTS [7]				ECSSD [131]				DUT [132]				HKU-IS [133]				PASCAL-S [134]				SOD [135]			
	$S_\alpha \uparrow$	$F_\beta \uparrow$	$E_\xi \uparrow$	$\mathcal{M} \downarrow$	$S_\alpha \uparrow$	$F_\beta \uparrow$	$E_\xi \uparrow$	$\mathcal{M} \downarrow$	$S_\alpha \uparrow$	$F_\beta \uparrow$	$E_\xi \uparrow$	$\mathcal{M} \downarrow$	$S_\alpha \uparrow$	$F_\beta \uparrow$	$E_\xi \uparrow$	$\mathcal{M} \downarrow$	$S_\alpha \uparrow$	$F_\beta \uparrow$	$E_\xi \uparrow$	$\mathcal{M} \downarrow$	$S_\alpha \uparrow$	$F_\beta \uparrow$	$E_\xi \uparrow$	$\mathcal{M} \downarrow$
B'_cnn	.882	.840	.916	.037	.922	.919	.947	.035	.823	.742	.851	.057	.912	.901	.947	.030	.855	.841	.896	.065	.832	.825	.863	.073
CIGAN	.876	.820	.906	.042	.923	.913	.945	.037	.823	.733	.848	.061	.911	.892	.943	.034	.856	.836	.893	.068	.833	.816	.862	.075
B'_tr	.911	.882	.947	.026	.939	.940	.965	.024	.860	.801	.894	.045	.927	.921	.964	.023	.876	.872	.917	.053	.858	.853	.897	.059
TIGAN	.909	.873	.941	.028	.941	.936	.964	.025	.861	.796	.890	.047	.929	.918	.962	.025	.879	.869	.916	.054	.861	.854	.894	.060
Performing FGSM [147] Attack																								
AB'_cnn	.782	.709	.824	.082	.837	.829	.874	.078	.714	.594	.744	.113	.838	.818	.889	.061	.771	.747	.819	.113	.713	.680	.747	.134
ACIGAN	.786	.692	.813	.092	.858	.833	.883	.076	.730	.601	.753	.119	.853	.814	.887	.065	.789	.758	.824	.113	.737	.690	.774	.136
AB'_tr	.802	.744	.872	.065	.844	.840	.898	.068	.746	.652	.808	.093	.840	.823	.910	.056	.779	.759	.842	.100	.746	.734	.807	.113
ATIGAN	.881	.837	.921	.040	.916	.912	.946	.037	.841	.773	.879	.056	.909	.897	.950	.033	.856	.851	.899	.067	.848	.847	.891	.067
Performing Adversarial Training [148] based Defense																								
DB'_cnn	.822	.761	.862	.063	.872	.868	.906	.059	.756	.649	.786	.088	.870	.855	.916	.047	.806	.787	.850	.093	.765	.740	.798	.105
DCIGAN	.838	.775	.872	.059	.891	.881	.918	.053	.781	.676	.808	.084	.886	.866	.922	.044	.826	.806	.867	.088	.783	.759	.819	.104
DB'_tr	.861	.822	.909	.045	.902	.905	.939	.041	.802	.726	.845	.070	.893	.887	.941	.036	.827	.819	.877	.078	.797	.793	.842	.090
DTIGAN	.906	.874	.942	.030	.939	.938	.964	.025	.864	.806	.898	.048	.929	.921	.964	.024	.873	.869	.915	.056	.866	.866	.903	.058



Fig. 11. Model robustness to adversarial attack, *i.e.* FGSM [147] attack, where the samples (from left to right) within each method (CIGAN and TIGAN) are the prediction of x , the adversarial sample x_{adv} , its prediction s_{adv} , and the prediction of x_{adv} after adversarial training.

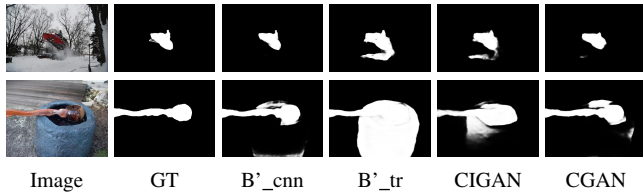


Fig. 12. Failure cases of the transformer backbone compared with the CNN backbone (B'_cnn and B'_tr), and iGAN compared with CGAN within the CNN backbone (CIGAN and CGAN) for RGB SOD.

based frameworks (CIGAN and TIGAN in Table 8). Specifically, based on the above models, we set $\epsilon = 8/255$ in Eq. (15) following [147] to generate adversarial samples x_{adv} of each training image, which will be used to train the above models again together with the clean sample x to achieve the defense process. We report model performance in Table 14. Note that the performance of attacked models is obtained by performing FGSM [147] attack on the testing samples, where the adversarial testing samples are fed to the specific model to generate the predictions. We show in Fig. 11 the clean sample x and its prediction s , the adversarial sample x_{adv} and its prediction s_{adv} , and the prediction of x and x_{adv} after the defense. Fig. 11 and Table 14 show that invisible adversarial attack [147] can cause significant performance degradation, which can be partially solved with the adversarial training strategies [148]. We also observe the slightly robust performance of the proposed iGAN frameworks (CIGAN and TIGAN) compared with the baseline models, which further explain the robustness of the proposed generative model.

Failure Case Analysis: To further investigate the limitations of both the transformer backbone and the iGAN framework, we look deeper in Table 8 and Table 9, and the predictions of each related model. We find out two main issues: 1) the transformer backbone does not always perform superior to the CNN backbone; 2) our iGAN model can lead to over-smoothed predictions compared

with CGAN due to the diverse generation process.

For the former, to exclude the influence of the iGAN framework, we compare the predictions of the CNN backbone (B'_cnn) and transformer backbone (B'_tr) for RGB SOD, and show samples in Fig. 12. We observe more false positives within B'_tr, which can be explained as the “double-edged sword” of the transformer backbone. On the one hand, the larger receptive field of the transformer makes it superior in localizing the larger salient foreground. On the other hand, the less salient objects that expand for a larger region can be falsely detected as positive foreground. We argue that salient object ranking [160] can be beneficial in identifying the less salient regions by providing extra saliency degree evaluation. For the latter, as the latent variable z within iGAN is conditioned on input x , leading to informative latent space, where the predictive distribution $p(y^*|x^*, \theta, z)$ for input x^* has larger variance compared with the CGAN based framework. In this case, the averaged prediction is over-smoothed. Similarly, this issue can also be fixed with saliency ranking [160].

5 CONCLUSION AND FUTURE WORK

In this paper, we proposed an inferential GAN within the transformer framework for both fully and weakly supervised SOD. Different from typical GANs that define the prior distribution as a standard normal distribution, we inferred the latent variable via Langevin Dynamics [37], a gradient based MCMC, leading to the image-conditioned prior distribution. Through extensive experiments, we observed that a larger receptive field of the transformer leads to its better performance on images with larger salient objects (see Fig. 6). However, we also found the double-edged sword effect of the larger receptive field that leads to serious false positives (see Fig. 12). Further, for RGB-D SOD, we found that the various depth sensors lead to a domain gap between the training dataset and the testing dataset (see Table 1 and Fig. 2). We then presented auxiliary depth module, leading to consistent depth contribution (see Table 7). For weakly supervised SOD,

we observed that the accurate structure information encoded in the transformer backbone as shown in Fig. 8 makes it powerful in generating structure-preserving predictions (see Table 10). Extensive experimental results demonstrate the superiority of our transformer backbone-based generative network, achieving new benchmarks with reliable uncertainty maps.

Our proposed generative model aims to estimate the reliability of saliency prediction with uncertainty maps, which also show superiority in achieving robust models (see Table 14 and Fig. 11) and well calibrated models (see Table 6). Our future work includes two main parts. Firstly, we will apply the produced uncertainty map (see Fig. 7) to the saliency generator for effective hard negative mining. In this way, the uncertainty map can not only explain model predictions but also serve as an important prior for effective model learning. Secondly, we have several hyper-parameters within the inference model, and we observe that our model performance can be influenced by them. We plan to further investigate model performance w.r.t.those hyper-parameters.

ACKNOWLEDGMENT

This work was partly supported by the National Natural Science Foundation of China (62271410, 61871325).

REFERENCES

- [1] M. Zhuge, D.-P. Fan, N. Liu, D. Zhang, D. Xu, and L. Shao, "Salient object detection via integrity learning," *IEEE TPAMI*, 2023.
- [2] Z. Wu, L. Su, and Q. Huang, "Stacked cross refinement network for edge-aware salient object detection," in *IEEE ICCV*, 2019.
- [3] J. Wei, S. Wang, and Q. Huang, "F³net: Fusion, feedback and focus for salient object detection," in *AAAI*, 2020.
- [4] J. Zhang, D.-P. Fan, Y. Dai, S. Anwar, F. Saleh, S. Aliakbarian, and N. Barnes, "Uncertainty inspired rgb-d saliency detection," *IEEE TPAMI*, vol. 44, no. 9, pp. 5761–5779, 2022.
- [5] D.-P. Fan, Y. Zhai, A. Borji, J. Yang, and L. Shao, "BBS-Net: RGB-D salient object detection with a bifurcated backbone strategy network," in *ECCV*, 2020.
- [6] J. Zhang, X. Yu, A. Li, P. Song, B. Liu, and Y. Dai, "Weakly-supervised salient object detection via scribble annotations," in *IEEE CVPR*, 2020.
- [7] L. Wang, H. Lu, Y. Wang, M. Feng, D. Wang, B. Yin, and X. Ruan, "Learning to detect salient objects with image-level supervision," in *IEEE CVPR*, 2017.
- [8] W. Wang, Q. Lai, H. Fu, J. Shen, H. Ling, and R. Yang, "Salient object detection in the deep learning era: An in-depth survey," *IEEE TPAMI*, vol. 44, no. 6, pp. 3239–3259, 2022.
- [9] J. Zhang, T. Zhang, Y. Dai, M. Harandi, and R. Hartley, "Deep unsupervised saliency detection: A multiple noisy labeling perspective," in *IEEE CVPR*, 2018.
- [10] D. T. Nguyen, M. Dax, C. K. Mummadi, T. P. N. Ngo, T. H. P. Nguyen, Z. Lou, and T. Brox, "DeepUSPS: Deep robust unsupervised saliency prediction with self-supervision," in *NeurIPS*, 2019.
- [11] M. Zhang, T. Liu, Y. Piao, S. Yao, and H. Lu, "Auto-msfnet: Search multi-scale fusion network for salient object detection," in *ACM MM*, 2021.
- [12] B. Xu, H. Liang, R. Liang, and P. Chen, "Locate globally, segment locally: A progressive architecture with knowledge review network for salient object detection," in *AAAI*, 2021.
- [13] Y.-H. Wu, Y. Liu, L. Zhang, M.-M. Cheng, and B. Ren, "Edn: Salient object detection via extremely-downsampled network," *IEEE TIP*, vol. 31, pp. 3125–3136, 2022.
- [14] Z. Yang, S. Soltanian-Zadeh, and S. Farsiu, "Biconnet: an edge-preserved connectivity-based approach for salient object detection," *Pattern Recognition*, vol. 121, p. 108231, 2022.
- [15] Y. Piao, W. Ji, J. Li, M. Zhang, and H. Lu, "Depth-induced multi-scale recurrent attention network for saliency detection," in *IEEE ICCV*, 2019.
- [16] K. Fu, D.-P. Fan, G.-P. Ji, and Q. Zhao, "JL-DCF: Joint learning and densely-cooperative fusion framework for RGB-D salient object detection," in *IEEE CVPR*, 2020.
- [17] J. Zhang, D.-P. Fan, Y. Dai, X. Yu, Y. Zhong, N. Barnes, and L. Shao, "Rgb-d saliency detection via cascaded mutual information minimization," in *IEEE ICCV*, 2021.
- [18] K. He, X. Zhang, S. Ren, and J. Sun, "Deep residual learning for image recognition," in *IEEE CVPR*, 2016.
- [19] Y. Niu, Y. Geng, X. Li, and F. Liu, "Leveraging stereopsis for saliency analysis," in *IEEE CVPR*, 2012.
- [20] C. Liu, J. Yuen, and A. Torralba, "Sift flow: Dense correspondence across scenes and its applications," *IEEE TPAMI*, vol. 33, no. 5, pp. 978–994, 2010.
- [21] H. Peng, B. Li, W. Xiong, W. Hu, and R. Ji, "RGBD salient object detection: A benchmark and algorithms," in *ECCV*, 2014.
- [22] Z. Zhang, "Microsoft kinect sensor and its effect," *IEEE multimedia*, vol. 19, no. 2, pp. 4–10, 2012.
- [23] Y. Cheng, H. Fu, X. Wei, J. Xiao, and X. Cao, "Depth enhanced saliency detection method," in *ICIMCS*, 2014.
- [24] R. Ju, Y. Liu, T. Ren, L. Ge, and G. Wu, "Depth-aware salient object detection using anisotropic center-surround difference," *Signal Processing: Image Communication*, vol. 38, pp. 115–126, 2015.
- [25] D. Sun, S. Roth, and M. J. Black, "Secrets of optical flow estimation and their principles," in *IEEE CVPR*, 2010.
- [26] N. Li, J. Ye, Y. Ji, H. Ling, and J. Yu, "Saliency detection on light field," in *IEEE CVPR*, 2014.
- [27] R. Ng, M. Levoy, M. Brédif, G. Duval, M. Horowitz, and P. Hanrahan, *Light field photography with a hand-held plenoptic camera*. PhD thesis, Stanford University, 2005.
- [28] D.-P. Fan, Z. Lin, Z. Zhang, M. Zhu, and M.-M. Cheng, "Rethinking RGB-D Salient Object Detection: Models, Datasets, and Large-Scale Benchmarks," *IEEE TNNLS*, vol. 32, no. 5, pp. 2075–2089, 2020.
- [29] K. Simonyan and A. Zisserman, "Very deep convolutional networks for large-scale image recognition," in *ICLR*, 2015.
- [30] Z. Wu, L. Su, and Q. Huang, "Cascaded partial decoder for fast and accurate salient object detection," in *IEEE CVPR*, 2019.
- [31] J. Kim, D. Han, Y.-W. Tai, and J. Kim, "Salient region detection via high-dimensional color transform and local spatial support," *IEEE TIP*, vol. 25, no. 1, pp. 9–23, 2015.
- [32] A. Vaswani, N. Shazeer, N. Parmar, J. Uszkoreit, L. Jones, A. N. Gomez, L. Kaiser, and I. Polosukhin, "Attention is all you need," in *NeurIPS*, 2017.
- [33] R. Ranftl, A. Bochkovskiy, and V. Koltun, "Vision transformers for dense prediction," in *IEEE ICCV*, 2021.
- [34] Z. Liu, Y. Lin, Y. Cao, H. Hu, Y. Wei, Z. Zhang, S. Lin, and B. Guo, "Swin transformer: Hierarchical vision transformer using shifted windows," in *IEEE ICCV*, 2021.
- [35] C. Guo, G. Pleiss, Y. Sun, and K. Q. Weinberger, "On calibration of modern neural networks," in *ICML*, 2017.
- [36] I. Goodfellow, J. Pouget-Abadie, M. Mirza, B. Xu, D. Warde-Farley, S. Ozair, A. Courville, and Y. Bengio, "Generative adversarial nets," in *NeurIPS*, 2014.
- [37] R. Neal, "Mcmc using hamiltonian dynamics," *Handbook of Markov Chain Monte Carlo*, 2011.
- [38] T. Han, Y. Lu, S.-C. Zhu, and Y. N. Wu, "Alternating back-propagation for generator network," in *AAAI*, 2017.
- [39] A. Kendall and Y. Gal, "What uncertainties do we need in bayesian deep learning for computer vision?," in *NeurIPS*, 2017.
- [40] S. Cao and Z. Zhang, "Deep hybrid models for out-of-distribution detection," in *IEEE CVPR*, 2022.
- [41] A. Dosovitskiy, L. Beyer, A. Kolesnikov, D. Weissenborn, X. Zhai, T. Unterthiner, M. Dehghani, M. Minderer, G. Heigold, S. Gelly, J. Uszkoreit, and N. Houlsby, "An image is worth 16x16 words: Transformers for image recognition at scale," in *ICLR*, 2021.
- [42] L. Itti, C. Koch, and E. Niebur, "A model of saliency-based visual attention for rapid scene analysis," *IEEE TPAMI*, vol. 20, no. 11, pp. 1254–1259, 1998.
- [43] M.-M. Cheng, N. J. Mitra, X. Huang, P. H. Torr, and S.-M. Hu, "Global contrast based salient region detection," *IEEE TPAMI*, vol. 37, no. 3, pp. 569–582, 2014.
- [44] O. Ronneberger, P. Fischer, and T. Brox, "U-net: Convolutional networks for biomedical image segmentation," in *MICCAI*, 2015.
- [45] Z. Luo, A. Mishra, A. Achkar, J. Eichel, S. Li, and P.-M. Jodoin, "Non-local deep features for salient object detection," in *IEEE CVPR*, 2017.
- [46] N. Liu, J. Han, and M.-H. Yang, "Picanet: Learning pixel-wise contextual attention for saliency detection," in *IEEE CVPR*, 2018.
- [47] B. Wang, Q. Chen, M. Zhou, Z. Zhang, X. Jin, and K. Gai, "Progressive feature polishing network for salient object detection," in *AAAI*, 2020.
- [48] Q. Hou, M.-M. Cheng, X. Hu, A. Borji, Z. Tu, and P. H. Torr, "Deeply supervised salient object detection with short connections," in *IEEE CVPR*, 2017.

- [49] T. Wang, A. Borji, L. Zhang, P. Zhang, and H. Lu, "A stagewise refinement model for detecting salient objects in images," in *IEEE ICCV*, 2017.
- [50] X. Zhao, Y. Pang, L. Zhang, H. Lu, and L. Zhang, "Suppress and balance: A simple gated network for salient object detection," in *ECCV*, 2020.
- [51] Z. Chen, Q. Xu, R. Cong, and Q. Huang, "Global context-aware progressive aggregation network for salient object detection," in *AAAI*, 2020.
- [52] W. Zhang, L. Zheng, H. Wang, X. Wu, and X. Li, "Saliency hierarchy modeling via generative kernels for salient object detection," in *ECCV*, 2022.
- [53] X. Qin, Z. Zhang, C. Huang, C. Gao, M. Dehghan, and M. Jagersand, "Basnet: Boundary-aware salient object detection," in *IEEE CVPR*, 2019.
- [54] Y. Pang, X. Zhao, L. Zhang, and H. Lu, "Multi-scale interactive network for salient object detection," in *IEEE CVPR*, 2020.
- [55] L. Tang, B. Li, Y. Zhong, S. Ding, and M. Song, "Disentangled high quality salient object detection," in *IEEE ICCV*, 2021.
- [56] S. Xie and Z. Tu, "Holistically-nested edge detection," in *IEEE ICCV*, 2015.
- [57] Y. Liu, M.-M. Cheng, X. Hu, K. Wang, and X. Bai, "Richer convolutional features for edge detection," in *IEEE CVPR*, 2017.
- [58] X. Qin, Z. Zhang, C. Huang, C. Gao, M. Dehghan, and M. Jagersand, "BASNet: Boundary-aware salient object detection," in *IEEE CVPR*, 2019.
- [59] J.-X. Zhao, J.-J. Liu, D.-P. Fan, Y. Cao, J. Yang, and M.-M. Cheng, "EGNet: edge guidance network for salient object detection," in *IEEE ICCV*, 2019.
- [60] X. Zhang, T. Wang, J. Qi, H. Lu, and G. Wang, "Progressive attention guided recurrent network for salient object detection," in *IEEE CVPR*, 2018.
- [61] M. Zhang, T. Liu, Y. Piao, S. Yao, and H. Lu, "Auto-msfnet: Search multi-scale fusion network for salient object detection," in *ACM MM*, 2021.
- [62] J. Han, H. Chen, N. Liu, C. Yan, and X. Li, "Cnns-based rgb-d saliency detection via cross-view transfer and multiview fusion," *IEEE Transactions on Cybernetics*, vol. 48, no. 11, pp. 3171–3183, 2017.
- [63] M. Lee, C. Park, S. Cho, and S. Lee, "Spsn: Superpixel prototype sampling network for rgb-d salient object detection," in *ECCV*, 2022.
- [64] L. Qu, S. He, J. Zhang, J. Tian, Y. Tang, and Q. Yang, "RGBD salient object detection via deep fusion," *IEEE TIP*, vol. 26, no. 5, pp. 2274–2285, 2017.
- [65] N. Wang and X. Gong, "Adaptive fusion for RGB-D salient object detection," *IEEE Access*, vol. 7, pp. 55277–55284, 2019.
- [66] J. Han, H. Chen, N. Liu, C. Yan, and X. Li, "CNNs-based RGB-D saliency detection via cross-view transfer and multiview fusion," *IEEE TOC*, vol. 48, no. 11, pp. 3171–3183, 2017.
- [67] Y. Piao, Z. Rong, M. Zhang, W. Ren, and H. Lu, "A2dele: Adaptive and attentive depth distiller for efficient RGB-D salient object detection," in *IEEE CVPR*, 2020.
- [68] H. Chen and Y. Li, "Progressively complementarity-aware fusion network for RGB-D salient object detection," in *IEEE CVPR*, 2018.
- [69] H. Chen, Y. Li, and D. Su, "Multi-modal fusion network with multi-scale multi-path and cross-modal interactions for RGB-D salient object detection," *Pattern Recognition*, vol. 86, pp. 376–385, 2019.
- [70] H. Chen and Y. Li, "Three-stream attention-aware network for RGB-D salient object detection," *IEEE TIP*, vol. 28, no. 6, pp. 2825–2835, 2019.
- [71] J.-X. Zhao, Y. Cao, D.-P. Fan, M.-M. Cheng, X.-Y. Li, and L. Zhang, "Contrast prior and fluid pyramid integration for RGBD salient object detection," in *IEEE CVPR*, 2019.
- [72] M. Zhang, W. Ren, Y. Piao, Z. Rong, and H. Lu, "Select, supplement and focus for RGB-D saliency detection," in *IEEE CVPR*, 2020.
- [73] N. Liu, N. Zhang, L. Shao, and J. Han, "Learning selective mutual attention and contrast for rgb-d saliency detection," *IEEE TPAMI*, vol. 44, no. 12, pp. 9026–9042, 2022.
- [74] W. Ji, J. Li, M. Zhang, Y. Piao, and H. Lu, "Accurate RGB-D salient object detection via collaborative learning," in *ECCV*, 2020.
- [75] Y. Pang, L. Zhang, X. Zhao, and H. Lu, "Hierarchical dynamic filtering network for RGB-D salient object detection," in *ECCV*, 2020.
- [76] Z. Zhang, Z. Lin, J. Xu, W.-D. Jin, S.-P. Lu, and D.-P. Fan, "Bilateral attention network for RGB-D salient object detection," *IEEE TIP*, vol. 30, pp. 1949–1961, 2021.
- [77] C. Li, R. Cong, Y. Piao, Q. Xu, and C. C. Loy, "RGB-D salient object detection with cross-modality modulation and selection," in *ECCV*, 2020.
- [78] G. Li, Z. Liu, L. Ye, Y. Wang, and H. Ling, "Cross-modal weighting network for RGB-D salient object detection," in *ECCV*, 2020.
- [79] A. Luo, X. Li, F. Yang, Z. Jiao, H. Cheng, and S. Lyu, "Cascade graph neural networks for RGB-D salient object detection," in *ECCV*, 2020.
- [80] S. Chen and Y. Fu, "Progressively guided alternate refinement network for RGB-D salient object detection," in *ECCV*, 2020.
- [81] M. Zhang, S. X. Fei, J. Liu, S. Xu, Y. Piao, and H. Lu, "Asymmetric two-stream architecture for accurate RGB-D saliency detection," in *ECCV*, 2020.
- [82] G. Li, Z. Liu, M. Chen, Z. Bai, W. Lin, and H. Ling, "Hierarchical alternate interaction network for rgb-d salient object detection," *IEEE TIP*, vol. 30, pp. 3528–3542, 2021.
- [83] K. Fu, D.-P. Fan, G.-P. Ji, Q. Zhao, J. Shen, and C. Zhu, "Siamese network for rgb-d salient object detection and beyond," *IEEE TPAMI*, vol. 44, no. 9, pp. 5541–5559, 2022.
- [84] N. Carion, F. Massa, G. Synnaeve, N. Usunier, A. Kirillov, and S. Zagoruyko, "End-to-end object detection with transformers," in *ECCV*, 2020.
- [85] X. Zhu, W. Su, L. Lu, B. Li, X. Wang, and J. Dai, "Deformable DETR: Deformable transformers for end-to-end object detection," in *ICLR*, 2021.
- [86] Z. Dai, B. Cai, Y. Lin, and J. Chen, "UP-DETR: Unsupervised pre-training for object detection with transformers," in *IEEE CVPR*, 2021.
- [87] W. Wang, E. Xie, X. Li, D.-P. Fan, K. Song, D. Liang, T. Lu, P. Luo, and L. Shao, "Pyramid vision transformer: A versatile backbone for dense prediction without convolutions," in *IEEE ICCV*, 2021.
- [88] G. Zhang, Z. Luo, K. Cui, S. Lu, and E. P. Xing, "Meta-detr: Image-level few-shot detection with inter-class correlation exploitation," *IEEE TPAMI*, 2022.
- [89] Y. Xu, Y. Ban, G. Delorme, C. Gan, D. Rus, and X. Alameda-Pineda, "Transcenter: Transformers with dense representations for multiple-object tracking," *IEEE TPAMI*, 2022.
- [90] B. Yan, H. Peng, J. Fu, D. Wang, and H. Lu, "Learning spatio-temporal transformer for visual tracking," in *IEEE ICCV*, 2021.
- [91] W. Mao, Y. Ge, C. Shen, Z. Tian, X. Wang, Z. Wang, and A. v. den Hengel, "Poseur: Direct human pose estimation with transformers," in *ECCV*, 2022.
- [92] S. Jiang, D. Campbell, Y. Lu, H. Li, and R. Hartley, "Learning to estimate hidden motions with global motion aggregation," in *IEEE ICCV*, 2021.
- [93] S. Zheng, J. Lu, H. Zhao, X. Zhu, Z. Luo, Y. Wang, Y. Fu, J. Feng, T. Xiang, P. H. Torr, and L. Zhang, "Rethinking semantic segmentation from a sequence-to-sequence perspective with transformers," in *IEEE CVPR*, 2021.
- [94] N. Liu, N. Zhang, K. Wan, L. Shao, and J. Han, "Visual saliency transformer," in *IEEE ICCV*, 2021.
- [95] J. Zhang, J. Xie, N. Barnes, and P. Li, "Learning generative vision transformer with energy-based latent space for saliency prediction," in *NeurIPS*, 2021.
- [96] D. Kingma and M. Welling, "Auto-encoding variational bayes," in *ICLR*, 2014.
- [97] Y. LeCun, S. Chopra, R. Hadsell, M. Ranzato, and F. Huang, "A tutorial on energy-based learning," *Predicting structured data*, vol. 1, no. 0, 2006.
- [98] K. Sohn, H. Lee, and X. Yan, "Learning structured output representation using deep conditional generative models," in *NeurIPS*, 2015.
- [99] C. F. Baumgartner, K. C. Tezcan, K. Chaitanya, A. M. Hötter, U. J. Muehlemaier, K. Schawkat, A. S. Becker, O. Donati, and E. Konukoglu, "Phiseg: Capturing uncertainty in medical image segmentation," in *MICCAI*, 2019.
- [100] S. Kohl, B. Romera-Paredes, C. Meyer, J. De Fauw, J. R. Ledsam, K. Maier-Hein, S. M. A. Eslami, D. Jimenez Rezende, and O. Ronneberger, "A probabilistic u-net for segmentation of ambiguous images," in *NeurIPS*, 2018.
- [101] B. Li, Z. Sun, and Y. Guo, "Supervae: Superpixelwise variational autoencoder for salient object detection," in *AAAI*, 2019.
- [102] R. Groenendijk, S. Karaoglu, T. Gevers, and T. Mensink, "On the benefit of adversarial training for monocular depth estimation," *CVIU*, vol. 190, p. 102848, 2020.
- [103] Q. H. Le, K. Youcef-Toumi, D. Tsetserukou, and A. Jahanian, "Gan mask r-cnn: instance semantic segmentation benefits from generative adversarial networks," in *NeurIPS Workshop*, 2020.
- [104] N. Souly, C. Spampinato, and M. Shah, "Semi supervised semantic segmentation using generative adversarial network," in *IEEE ICCV*, 2017.

- [105] W.-C. Hung, Y.-H. Tsai, Y.-T. Liou, Y.-Y. Lin, and M.-H. Yang, "Adversarial learning for semi-supervised semantic segmentation," in *BMVC*, 2018.
- [106] Y. Chen, Q. Gao, X. Wang, *et al.*, "Inferential wasserstein generative adversarial networks," *Journal of the Royal Statistical Society Series B*, vol. 84, no. 1, pp. 83–113, 2022.
- [107] J. He, D. Spokoiny, G. Neubig, and T. Berg-Kirkpatrick, "Lagging inference networks and posterior collapse in variational autoencoders," in *ICLR*, 2019.
- [108] K.-J. Hsu^{1,2}, Y.-Y. Lin, and Y.-Y. Chuang, "Weakly supervised saliency detection with a category-driven map generator," *BMVC*, 2017.
- [109] G. Li, Y. Xie, and L. Lin, "Weakly supervised salient object detection using image labels," in *AAAI*, 2018.
- [110] J. Ahn and S. Kwak, "Learning pixel-level semantic affinity with image-level supervision for weakly supervised semantic segmentation," in *IEEE CVPR*, 2018.
- [111] Z. Huang, X. Wang, J. Wang, W. Liu, and J. Wang, "Weakly-supervised semantic segmentation network with deep seeded region growing," in *IEEE CVPR*, 2018.
- [112] H. Zhang, Y. Zeng, H. Lu, L. Zhang, J. Li, and J. Qi, "Learning to detect salient object with multi-source weak supervision," *IEEE TPAMI*, vol. 44, no. 7, pp. 3577–3589, 2022.
- [113] C. Song, Y. Huang, W. Ouyang, and L. Wang, "Box-driven class-wise region masking and filling rate guided loss for weakly supervised semantic segmentation," in *IEEE CVPR*, 2019.
- [114] J. Dai, K. He, and J. Sun, "Boxsup: Exploiting bounding boxes to supervise convolutional networks for semantic segmentation," in *IEEE ICCV*, 2015.
- [115] V. Kulharia, S. Chandra, A. Agrawal, P. Torr, and A. Tyagi, "Box2seg: Attention weighted loss and discriminative feature learning for weakly supervised segmentation," in *ECCV*, 2020.
- [116] J. Lee, J. Yi, C. Shin, and S. Yoon, "Bbam: Bounding box attribution map for weakly supervised semantic and instance segmentation," in *IEEE CVPR*, 2021.
- [117] Z. Tian, C. Shen, X. Wang, and H. Chen, "Boxinst: High-performance instance segmentation with box annotations," in *IEEE CVPR*, 2021.
- [118] D. Lin, J. Dai, J. Jia, K. He, and J. Sun, "Scribblesup: Scribble-supervised convolutional networks for semantic segmentation," in *IEEE CVPR*, 2016.
- [119] P. Vernaza and M. Chandraker, "Learning random-walk label propagation for weakly-supervised semantic segmentation," in *IEEE CVPR*, 2017.
- [120] S. Yu, B. Zhang, J. Xiao, and E. G. Lim, "Structure-consistent weakly supervised salient object detection with local saliency coherence," in *AAAI*, 2021.
- [121] A. Bearman, O. Russakovsky, V. Ferrari, and L. Fei-Fei, "What's the point: Semantic segmentation with point supervision," in *ECCV*, 2016.
- [122] H. Chen, J. Wang, H. C. Chen, X. Zhen, F. Zheng, R. Ji, and L. Shao, "Seminar learning for click-level weakly supervised semantic segmentation," in *IEEE ICCV*, 2021.
- [123] A. Obukhov, S. Georgoulis, D. Dai, and L. Van Gool, "Gated CRF loss for weakly supervised semantic image segmentation," in *NeurIPS*, 2019.
- [124] P. Arbeláez, J. Pont-Tuset, J. T. Barron, F. Marques, and J. Malik, "Multiscale combinatorial grouping," in *IEEE CVPR*, 2014.
- [125] C. Rother, V. Kolmogorov, and A. Blake, "'grabcut' interactive foreground extraction using iterated graph cuts," *ACM TOG*, vol. 23, no. 3, pp. 309–314, 2004.
- [126] J. Zhang, J. Xie, and N. Barnes, "Learning noise-aware encoder-decoder from noisy labels by alternating back-propagation for saliency detection," in *ECCV*, 2020.
- [127] Y. Zhang, K. Li, K. Li, L. Wang, B. Zhong, and Y. Fu, "Image super-resolution using very deep residual channel attention networks," in *ECCV*, 2018.
- [128] M. Yang, K. Yu, C. Zhang, Z. Li, and K. Yang, "Denseaspp for semantic segmentation in street scenes," in *IEEE CVPR*, 2018.
- [129] C. Godard, O. Mac Aodha, and G. J. Brostow, "Unsupervised monocular depth estimation with left-right consistency," in *IEEE CVPR*, 2017.
- [130] I. Higgins, L. Matthey, A. Pal, C. Burgess, X. Glorot, M. Botvinick, S. Mohamed, and A. Lerchner, "beta-VAE: Learning basic visual concepts with a constrained variational framework," in *ICLR*, 2017.
- [131] Q. Yan, L. Xu, J. Shi, and J. Jia, "Hierarchical saliency detection," in *IEEE CVPR*, 2013.
- [132] C. Yang, L. Zhang, H. Lu, X. Ruan, and M.-H. Yang, "Saliency detection via graph-based manifold ranking," in *IEEE CVPR*, 2013.
- [133] G. Li and Y. Yu, "Visual saliency based on multiscale deep features," in *IEEE CVPR*, 2015.
- [134] Y. Li, X. Hou, C. Koch, J. M. Rehg, and A. L. Yuille, "The secrets of salient object segmentation," in *IEEE CVPR*, 2014.
- [135] V. Movahedi and J. H. Elder, "Design and perceptual validation of performance measures for salient object segmentation," in *IEEE CVPR Workshop*, 2010.
- [136] H. Zhou, X. Xie, J.-H. Lai, Z. Chen, and L. Yang, "Interactive two-stream decoder for accurate and fast saliency detection," in *IEEE CVPR*, 2020.
- [137] Z. Zhao, C. Xia, C. Xie, and J. Li, "Complementary trilateral decoder for fast and accurate salient object detection," in *ACM MM*, 2021.
- [138] X. Li, F. Yang, H. Cheng, W. Liu, and D. Shen, "Contour knowledge transfer for salient object detection," in *ECCV*, 2018.
- [139] D.-P. Fan, C. Gong, Y. Cao, B. Ren, M.-M. Cheng, and A. Borji, "Enhanced-alignment measure for binary foreground map evaluation," in *IJCAI*, 2018.
- [140] D.-P. Fan, M.-M. Cheng, Y. Liu, T. Li, and A. Borji, "Structure-measure: A new way to evaluate foreground maps," in *IEEE ICCV*, 2017.
- [141] G. Franchi, X. Yu, A. Bursuc, E. Aldea, S. Dubuisson, and D. Filliat, "Latent discriminant deterministic uncertainty," in *ECCV*, 2022.
- [142] M. H. DeGroot and S. E. Fienberg, "The comparison and evaluation of forecasters," *Journal of the Royal Statistical Society: Series D (The Statistician)*, vol. 32, no. 1–2, pp. 12–22, 1983.
- [143] S. Depeweg, J.-M. Hernandez-Lobato, F. Doshi-Velez, and S. Udluft, "Decomposition of uncertainty in Bayesian deep learning for efficient and risk-sensitive learning," in *ICML*, 2018.
- [144] Y. Wang, Y. Yang, Z. Yang, L. Zhao, P. Wang, and W. Xu, "Occlusion aware unsupervised learning of optical flow," in *IEEE CVPR*, 2018.
- [145] M. Naseer, K. Ranasinghe, S. Khan, M. Hayat, F. S. Khan, and M.-H. Yang, "Intriguing properties of vision transformers," in *NeurIPS*, 2021.
- [146] J. Deng, W. Dong, R. Socher, L.-J. Li, K. Li, and L. Fei-Fei, "Imagenet: A large-scale hierarchical image database," in *IEEE CVPR*, 2009.
- [147] I. J. Goodfellow, J. Shlens, and C. Szegedy, "Explaining and harnessing adversarial examples," in *ICLR*, 2014.
- [148] A. Madry, A. Makelov, L. Schmidt, D. Tsipras, and A. Vladu, "Towards deep learning models resistant to adversarial attacks," in *ICLR*, 2018.
- [149] W. Wright, "Bayesian approach to neural-network modeling with input uncertainty," *IEEE TNN*, vol. 10, no. 6, pp. 1261–1270, 1999.
- [150] Y. Gal and Z. Ghahramani, "Bayesian convolutional neural networks with bernoulli approximate variational inference," *arXiv preprint arXiv:1506.02158*, 2015.
- [151] M. Vadera, B. Jalaian, and B. Marlin, "Generalized bayesian posterior expectation distillation for deep neural networks," in *CUAI*, 2020.
- [152] M. I. Jordan, Z. Ghahramani, and *et al.*, "An introduction to variational methods for graphical models," in *Machine Learning*, pp. 183–233, MIT Press, 1999.
- [153] M. J. Wainwright and M. I. Jordan, "Graphical models, exponential families, and variational inference," *Foundations and Trends® in Machine Learning*, vol. 1, no. 1–2, pp. 1–305, 2008.
- [154] S. Y. Lee, "Gibbs sampler and coordinate ascent variational inference: A set-theoretical review," *Communications in Statistics-Theory and Methods*, vol. 51, no. 6, pp. 1549–1568, 2022.
- [155] W. K. Hastings, "Monte Carlo sampling methods using Markov chains and their applications," *Biometrika*, vol. 57, pp. 97–109, 04 1970.
- [156] Y. Gal and Z. Ghahramani, "Dropout as a bayesian approximation: Representing model uncertainty in deep learning," in *ICML*, 2016.
- [157] A. Damianou and N. D. Lawrence, "Deep Gaussian processes," in *AISTATS*, 2013.
- [158] C. Szegedy, W. Zaremba, I. Sutskever, J. Bruna, D. Erhan, I. Goodfellow, and R. Fergus, "Intriguing properties of neural networks," in *ICLR*, 2014.
- [159] E. Wong and Z. Kolter, "Provable defenses against adversarial examples via the convex outer adversarial polytope," in *ICLR*, 2018.
- [160] M. A. Islam, M. Kalash, and N. D. Bruce, "Revisiting salient object detection: Simultaneous detection, ranking, and subitizing of multiple salient objects," in *IEEE CVPR*, 2018.